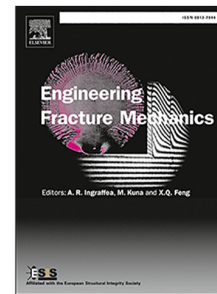


Journal Pre-proof

Characterisation of rate-dependent mode-II adhesive debonding based on a novel load–displacement curve parametrisation

Damjan Jurković, Leo Škec, Giulio Alfano



PII: S0013-7944(26)00458-3

DOI: <https://doi.org/10.1016/j.engfracmech.2026.112296>

Reference: EFM 112296

To appear in: *Engineering Fracture Mechanics*

Received date: 6 March 2026

Revised date: 6 May 2026

Accepted date: 18 May 2026

Please cite this article as: D. Jurković, L. Škec and G. Alfano, Characterisation of rate-dependent mode-II adhesive debonding based on a novel load–displacement curve parametrisation.

Engineering Fracture Mechanics (2026), doi: <https://doi.org/10.1016/j.engfracmech.2026.112296>.

This is a PDF of an article that has undergone enhancements after acceptance, such as the addition of a cover page and metadata, and formatting for readability. This version will undergo additional copyediting, typesetting and review before it is published in its final form. As such, this version is no longer the Accepted Manuscript, but it is not yet the definitive Version of Record; we are providing this early version to give early visibility of the article. Please note that Elsevier's sharing policy for the Published Journal Article applies to this version, see: <https://www.elsevier.com/about/policies-and-standards/sharing#4-published-journal-article>. Please also note that, during the production process, errors may be discovered which could affect the content, and all legal disclaimers that apply to the journal pertain.

© 2026 Published by Elsevier Ltd.

Characterisation of rate-dependent mode-II adhesive debonding based on a novel load-displacement curve parametrisation

Damjan Jurković^a, Leo Škec^a, Giulio Alfano^{b,*}

^a*Faculty of Civil Engineering, University of Rijeka, Radmile Matejčić 3, 51000 Rijeka, Croatia*

^b*Department of Engineering, Brunel University of London, Kingston Lane, Uxbridge UB8 3PH, UK*

Abstract

In this study, the mode-II rate dependence of an epoxy adhesive is investigated using end-notched flexure (ENF) tests conducted over loading speeds ranging from 0.1 to 5000 mm/min. To address the pronounced scatter typically observed in mode-II debonding tests, as well as the lack of a procedure for evaluation of the average load-displacement curve, a novel curve-parametrisation and statistical averaging framework is proposed. The load-displacement curves are represented using a set of parameters, enabling the construction of representative average curves for each loading speed and the quantification of parameter variability. The method allows the rate-dependent behaviour to be assessed over the entire load-displacement domain, rather than being restricted to the region typically used for the evaluation of the fracture resistance. The representative values of the critical energy release rate evaluated for each loading speed using the proposed method are in good agreement with the mean values obtained by a conventional specimen-by-specimen analysis. The results show a monotonic increase in mode-II fracture resistance with increasing loading speed, followed by a plateau at higher speeds. However, the proposed method reveals a continued monotonic evolution of the global response with loading speed, indicating

*Corresponding author

Email address: giulio.alfano@brunel.ac.uk (Giulio Alfano)

that rate-dependent effects extend beyond the critical energy release rate alone. These findings demonstrate that the proposed parametrisation framework enables statistically robust characterisation of rate-dependent mode-II adhesive debonding and improved constitutive modelling.

Keywords: adhesive joints, mode-II delamination, ENF experiment, fracture resistance, rate-dependent behaviour

Nomenclature

\bar{x}	Alternative x value for a second branch function
\hat{x}_i	x -coordinate values for which $S_i = 0.95$, $i = (1, 2)$
a	Crack length
a_0	Initial crack length
a_e	Equivalent crack length
a_{ij}	Branch functions' fitting parameters, $i, j = (1, 2, 3)$
b	Width of adherends
C	Specimen compliance
C_0	Initial measured specimen compliance
C_{0corr}	Initial measured specimen compliance corrected for shear deformation
C_{corr}	Measured specimen compliance corrected for shear deformation
C_{msr}	Measured specimen compliance
d	Thickness of adherends
E	Young's modulus

E_f	Flexural modulus of adherends
F	Applied load
F_i	Load at the characteristic points, $i = (12, 21, 22, 31, I, M, m, N)$
f_i	Branch functions, $i = (1, 2, 3)$
G_c	Critical energy release rate
G_m	Shear modulus of adherends
$G_{II,c}$	Critical energy release rate in mode II
I	Second moment of area
k_i	Rate of change of the logistic function, $i = (1, 2)$
L	Length of adherends
L_0	Span between the supports of an ENF specimen
p_F	Second branch domain factor
R^2	Coefficient of determination
S_i	Logistic function values, $i = (1, 2)$
t	Bondline thickness
v	Prescribed displacement
w_i	Weight functions, $i = (1, 2, 3)$
x	x -coordinate value
x_i	x -coordinates of the characteristic points, $i = (12, 21, 22, 31, I, M, m, N)$
x_w	Limiting x value for a second branch function
Δa_{DPZ}	Damage process zone length of influence

ΔF	Force drop
μ_i	Midpoint of the logistic function, $i = (1, 2)$
4ENF	4-Point End-Notched Flexure
ASTM	American Society for Testing and Materials
BSI	British Standards Institution
BTBR	Beam Theory with Bending Rotations
CBBM	Compliance-Based Beam Method
CBTE	Corrected Beam Theory with Effective Crack Length
CCM	Compliance Calibration Method
DCB	Double Cantilever Beam
ELS	End-Loaded Split
ENF	End-Notched Flexure
L-BFGS-B	Limited-memory Broyden–Fletcher–Goldfarb–Shanno with Bounds
LEFM	Linear-Elastic Fracture Mechanics
MSE	Mean Squared Error
TENF	Tapered End-Notched Flexure
UTM	Universal Testing Machine

1. Introduction

Adhesive joints are used as load-bearing structural connections in a wide range of applications in contemporary engineering. In these applications, they are subjected to a wide range of loading speeds, from creep to impact loading. Because many modern adhesives are based on synthetic polymers and are therefore sensitive to strain-rate effects, understanding their rate-dependent behaviour is of great importance. Moreover, studying adhesive debonding, as a critical failure mode of adhesive joints, is essential because it directly affects the reliability, durability and safety of adhesively bonded structures in engineering applications.

Adhesive debonding is commonly classified into three fundamental fracture modes: mode I (opening), mode II (in-plane shear) and mode III (out-of-plane shear), while practical joint failures often occur under mixed-mode loading conditions. The critical energy release rate (G_c) is a key parameter for characterising the fracture resistance of adhesive joints under different debonding modes.

Among many test procedures proposed for the determination of mode-II critical energy release rate $G_{II,c}$, the end-notched flexure (ENF) test [1] is the most widely used. Although commonly used for determining the properties of adhesive joints [2–4], the procedure is currently standardised by the ASTM [5] and BSI standards [6] only for fibre-reinforced polymer matrix composites.

Most data-reduction schemes used to calculate the critical energy release rate G_c are based on formulations combining simple beam theory and linear-elastic fracture mechanics (LEFM). Although the industrial standard for the ENF test [5] states that the Compliance Calibration Method (CCM) is the only acceptable data reduction method for the ENF test, several different methods have been proposed (a comparison of these methods is presented in [7]). The biggest drawback of CCM is that it requires an accurate measurement of the crack length, which is not straightforward for sudden crack propagation with crack faces pressed against each other in compression, especially at higher loading speeds. In addition, the ENF test does not produce a crack whose tip

31 can be clearly defined [8]. To avoid the measurement of the crack position, the
32 Compliance-Based Beam Method (CBBM) [3] and the Beam Theory with Bend-
33 ing Rotations (BTBR) [9] for the ENF test, and the Corrected Beam Theory
34 with Effective Crack Length (CBTE) for the ELS test [10] have been proposed
35 for the calculation of $G_{II,c}$. An additional advantage of the CBBM method is
36 that it does not require the measurement of any properties of the bulk material
37 (such as Young's modulus and shear modulus) for the determination of $G_{II,c}$.

38 As with most topics related to adhesive joints, the rate-dependent failure
39 behaviour has been studied more thoroughly for mode-I debonding than for
40 mode-II and mixed-mode debonding. A widely used standardised test for mode-
41 I debonding is the double cantilever beam (DCB) test, for which rate-dependent
42 analyses have been performed by several authors [11–13].

43 Only few robust rate-dependent analyses of mode-II debonding using the
44 ENF test have been reported in [14–19], typically within broader investigations
45 encompassing multiple debonding modes. The rate-dependent behaviour was
46 studied for the ENF test exclusively in [20] and for the tapered end-notched
47 flexure (TENF) test with stable crack propagation in [21, 22]. On the other
48 hand, most of these studies rely on a relatively small number of loading speeds
49 (typically 2 [17, 18, 21], 3 [14] or 4 [19, 20], with the exception of Refs. [16, 22]
50 in which 5 and 6 loading speeds, the latter in a TENF test setup).

51 There is also no clear consensus on the trend of rate-dependence of the
52 mode-II critical energy release rate for typical adhesives, as some authors found
53 an increase [16, 17, 20–22], while others found a decrease [18, 23] in fracture
54 resistance with an increase in loading speed. Moreover, it has been reported
55 in [19] that, using the same data-reduction scheme to evaluate $G_{II,c}$ from the
56 experimental measurements, the obtained values of $G_{II,c}$ at high-speed loads
57 can be higher or lower than those at quasi-static loading, depending on the
58 data acquisition method used. ENF tests that measured the strain rate in the
59 adhesive showed that, in experiments with a constant loading speed, the strain
60 rate in the process zone increases monotonically [14, 15]. In addition, in [14] it
61 was shown that $G_{II,c}$ increases with an increase in the strain rate.

62 ENF tests generally result in a lot of scatter in the load-displacement experi-
63 mental data, mostly concentrated in the region after the peak load, characterised
64 by a load drop and crack propagation. The scatter in the ENF load-displacement
65 diagrams becomes even more problematic in rate-dependent analysis, where the
66 diagrams of specimens tested at different loading speeds overlap, as can be seen
67 in [19]. This issue makes the determination of the average representative load-
68 displacement curve less straightforward than in the case of the DCB test [13].
69 No method has ever been proposed to produce physically realistic average load-
70 displacement curves so far in the literature. This is probably why numerical
71 models are commonly validated against experimental data by fitting the load-
72 displacement diagrams of individual ENF tests or by overlapping the results of
73 the numerical model onto the envelope of experimental results [18, 19, 22]. It
74 should be noted that this kind of scatter is not an artefact of the ENF test itself,
75 as it can also be found in alternative mode-II tests, such as the end-loaded split
76 (ELS) and the 4-point end-notched flexure (4ENF) tests [24].

77 The scatter in the load-displacement diagrams also translates into the scatter
78 of the determined values of the critical energy release rate. The typical proce-
79 dure for determining a representative value of $G_{II,c}$, as defined by the ASTM
80 standard [5] and commonly used in the literature [3, 24, 25], is to evaluate
81 it for each individual specimen and then calculate the mean value and stan-
82 dard deviation for the entire dataset. The same methodology is also adopted
83 for the analysis of rate-dependent experiments [16–22], where a mean value of
84 $G_{II,c}$ is calculated in this manner for each loading speed. It should be noted
85 that this approach for characterising the mode-II fracture resistance of adhesive
86 joints is limited exclusively to a relatively small post-peak region of the load-
87 displacement curve (in which most of the scatter is concentrated). However, the
88 remaining neglected portions of the load–displacement curve contain valuable
89 information on initial stiffness and softening and residual load-carrying capacity.
90 As will be shown later, by ignoring these regions, important insights into the
91 rate-dependent response and variability between specimens may be overlooked,
92 leading to an incomplete characterisation of mode-II debonding behaviour.

93 In this study, ENF experiments with varying loading speeds were performed
94 to characterise the rate-dependent mode-II fracture resistance of adhesive joints
95 made of aluminium flat bars bonded with an epoxy adhesive. Such a compre-
96 hensive experimental dataset, comprising 29 ENF tests conducted at six loading
97 speeds ranging from 0.1 to 5000 mm/min, provides a contribution to understand-
98 ing the rate-dependent behaviour of mode-II adhesive debonding across a larger
99 number of tested speeds than those considered in most studies, as previously
100 discussed. In particular, by using a finer resolution of speeds, one logarithmic
101 decade apart from each other, we can better capture the trend of rate depen-
102 dence.

103 Although a similar experimental analysis was previously conducted to char-
104 acterise mode-I rate-dependent fracture resistance using the DCB test [13], the
105 current analysis of the experimental data revealed several issues in obtaining a
106 reliable and accurate assessment of the rate-dependent properties of the adhe-
107 sive. First, it was noticed that relatively small differences in bondline thickness,
108 as well as bonding defects (such as voids and interfacial failure), can have a
109 significant influence on the results. Without investigating these effects in more
110 detail, a method has been proposed to select the most representative specimens
111 and discard the least representative, thus significantly reducing the scatter in
112 the experimental data.

113 An original robust approach has been developed to parametrise the load-
114 displacement curves, thus enabling the construction of representative average
115 load-displacement curves. When constructed as an average for each loading
116 speed, these curves can be used not only to directly determine the average value
117 of $G_{II,c}$ using the common data-reduction schemes, but can also provide ad-
118 ditional valuable information on the rate-dependent behaviour on the parts of
119 the load-displacement curve that are typically not considered in the charac-
120 terisation of the fracture resistance. Furthermore, the parametrisation of the
121 load-displacement curve allows for its quantitative assessment, paving the way
122 for an automated analysis of the experimental results, real-time identification
123 of the faulty specimens and improved constitutive modelling.

124 The outline of the paper is as follows. The experimental set-up used is de-
 125 scribed in Section 2, while Section 3 describes the post-processing of the exper-
 126 imental results and the novel averaging technique based on the parametrisation
 127 of the load-displacement curve. In Section 4, the presented method is verified by
 128 comparing the mean values of the critical energy release rate from the individual
 129 specimen analyses with those obtained from the parametrised average curves.
 130 Furthermore, additional insights into the rate-dependent behaviour provided by
 131 the proposed method are analysed and discussed. The last section summarises
 132 the main original contributions of the present work and discusses its potential
 133 for application and further development.

134 2. Experimental set up

135 In order to characterise the rate-dependent behaviour of an epoxy adhesive,
 136 specimens consisting of two Al 6082-T6 aluminium plates bonded together by
 137 a thin layer of Araldite[®] 2015 adhesive were manufactured and tested. Note
 138 that the same materials were also used for the specimens in a former analysis
 139 of rate-dependent behaviour in mode I [13]. The specimen geometry is shown
 140 in Figure 1, with dimensions reported in Table 1.

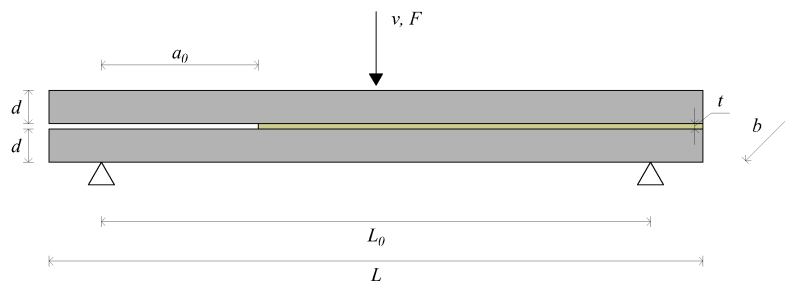


Figure 1: ENF test specimens geometry. Dimensions are reported in Table 1.

141 Specimen preparation followed the same procedure as in [13]. Bonding sur-
 142 faces of the aluminium plates were roughened using sand paper and afterwards
 143 cleaned using acetone. A thin aluminium foil was used to create a clear notch

Dimensions	L	L_0	d	b	a_0	t
Values [mm]	250	210	12.7	25.4	60	0.2

Table 1: Dimensions of the ENF specimens

144 edge at a distance a_0 from the left-hand support. A thin layer of adhesive was
 145 applied to the bonding surfaces using a cylindrical wooden stick and subse-
 146 quently evened out using a spatula. After applying the adhesive on both plates,
 147 they were joined together and clamped on both edges. Specimens were then
 148 pressed together by applying a 60 ± 10 N force for 60 s and subsequently left to
 149 cure at room temperature for 24 hours under the weight of a 1 kg mass. Both
 150 the force and the weight were evenly distributed over each specimen by means
 151 of a wooden bar. Finally, specimens were oven-cured for 60 min at 80°C .

152 After curing, specimens were left to cool down and their thicknesses were
 153 measured using a digital caliper with a resolution of 0.1 mm. Because spacers
 154 were not used during specimen preparation, the bondline thickness was deter-
 155 mined as the mean value of the difference between the total thickness of two
 156 aluminium adherends before and after bonding in three different points along
 157 the length. The resulting mean thickness was 0.19 mm, with a standard de-
 158 viation of 0.06 mm. The measured bondline thicknesses of all specimens are
 159 reported in Table A.3 in Appendix A.

160 Experiments were performed using an electromechanical Instron 5967 uni-
 161 versal testing machine (UTM) with 30-kN load cell (model 2580-202), except for
 162 tests at 5000 mm/min, which were performed using a 100-kN servo-hydraulic
 163 frame Instron 8501. Specimens were loaded in displacement control at six dif-
 164 ferent constant loading speeds, namely 0.1, 1, 10, 100, 1000 and 5000 mm/min
 165 and at least four specimens were tested for each speed. Specimens were labelled
 166 so that the first number indicates the loading speed used for testing, while the
 167 second number indicates the chronological order of the specimen tested at that
 168 loading speed. Specimen pre-cracking was not performed.

169 *2.1. Fracture plane assessment*

170 After inspection of the fracture surfaces, it was found that there are signif-
171 icant differences in the amount of voids and interfacial debonding present in
172 different specimens. To account for this, visual inspection of the fracture sur-
173 faces has been performed to divide the specimens into four groups, each group
174 characterised by a grade based on the bonding quality, with the void content
175 decreasing from grade 1 to 4. The bonding grade structure is defined as such
176 that each of the four grade groups contains a similar number of specimens, thus
177 separating the dataset into quartiles. The presence of interfacial debonding was
178 accounted for as a negative influence on the bonding quality by decreasing the
179 bonding grade accordingly. After the grading procedure was performed for all
180 specimens, all grade groups were cross-referenced to check for inconsistencies.
181 The assigned bonding grades for all specimens are reported in Table A.3 in
182 Appendix A.

183 Representative fracture planes for each of the bonding grades are shown in
184 Figure 2, where the coordinates along the length of each specimen are denoted
185 starting from the initial crack ($a_0 = 60$ mm). It is important to note that at the
186 end of the test the specimens were not fully detached, as for most specimens the
187 crack reached approximately the load-application point ($a \approx 105$ mm). Speci-
188 mens were therefore manually separated (in mode I), which can be recognised
189 in fracture-surface photos by a slight difference in colour and roughness on the
190 initial half of the crack surface. Consequently, only the initial half of the crack
191 surface was considered for the assessment of the bonding grade. On this part of
192 the fracture surface, the voids and interfacial failure are represented by darker
193 areas. In case of voids, these darker areas are present symmetrically on both
194 surfaces (top and bottom), whereas in case of interfacial failure, darker areas
195 (representing aluminium surface) are present only on one side. The broken
196 adhesive (by cohesive failure) is represented by lighter and rougher areas.

197 It can be seen that specimens in lower grades have considerably larger areas
198 with voids and interfacial failure than those in higher grades. Using this method-
199 ology, all four grades consist of seven specimens, except for the 2nd grade, which

200 consists of eight specimens. This resulted in a mean specimen grade equal to
 201 2.52. The proposed grading system can be considered as a qualitative counter-
 202 part to the void volume fraction in the bondline. Such measurements, performed
 203 by digital tomography, were presented in [23], showing that an increase in bond-
 204 line thickness results in a decrease in the void volume fraction and an increase
 205 in the fracture energy.

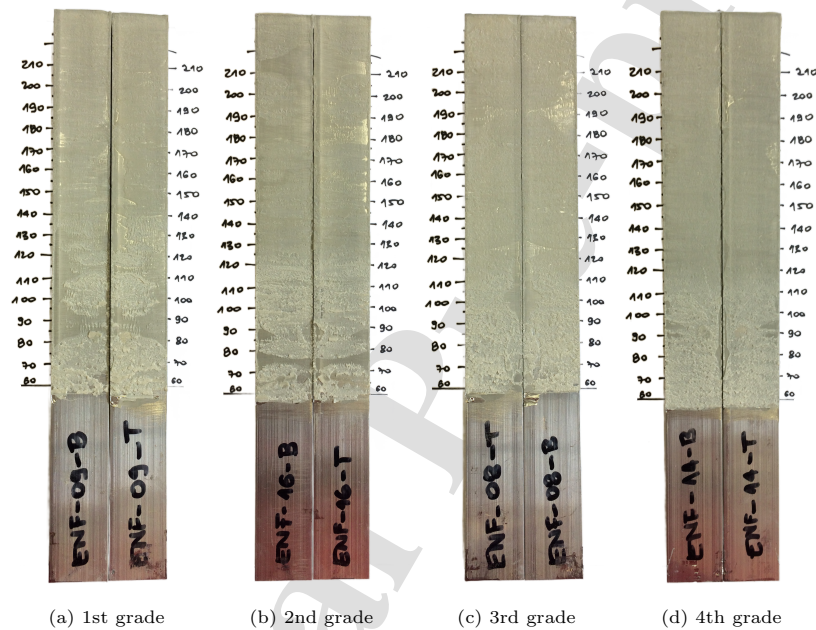


Figure 2: Representative fracture planes for each of the four bonding grades. Lower specimen grades correspond to higher amount of defects (voids and interfacial failure) and vice versa.

206 2.2. Dataset reduction

207 The analysis of the load-displacement curves revealed that several specimens
 208 behaved as outliers in their respective loading-rate groups. For this reason, the
 209 dataset was reduced so that each loading-rate group consisted of three represen-
 210 tative specimens, which is assumed to be a minimum number for a representative
 211 statistical sample. Specimens were discarded from the group if: i) their bondline
 212 thickness was significantly higher compared to the rest of the group or ii) their

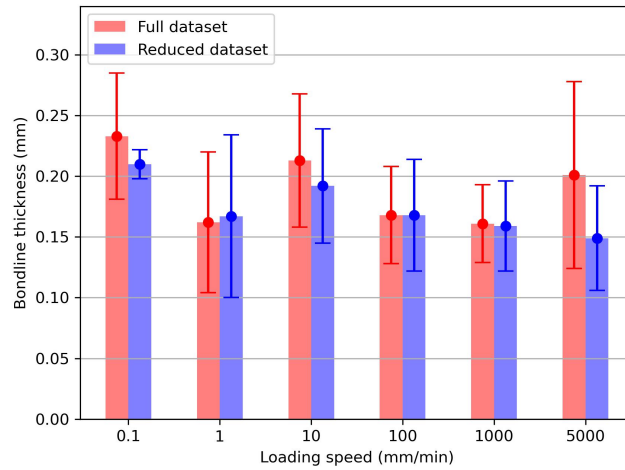
213 bonding grade was the lowest in the group. The discarded specimens, together
214 with the reason for their exclusion, are reported in Table A.3 in Appendix A.
215 In the rest of the paper, specimens that were not accounted for in the reduced
216 dataset will be marked accordingly and the presented procedure will be applied
217 to both reduced and full datasets. It should be noted that the mean bonding
218 grade and mean bondline thickness vary across the loading-speed groups. This
219 is true for both full and reduced datasets, whose mean values of thickness and
220 bonding grade are shown in Figure 3. It can be seen that the average thicknesses
221 for different loading-speed groups in the reduced dataset are far more uniform
222 than in the full dataset. The mean thickness of all loading-rate groups changed
223 from 0.19 mm with a standard deviation of 0.03 mm for the full dataset to 0.17
224 mm with a standard deviation of 0.02 mm for the reduced dataset. When it
225 comes to the mean bonding grade, dataset reduction process raised the mean
226 grade for the selected specimens from 2.52 to 2.56.

227 *2.3. Experimental data post-processing*

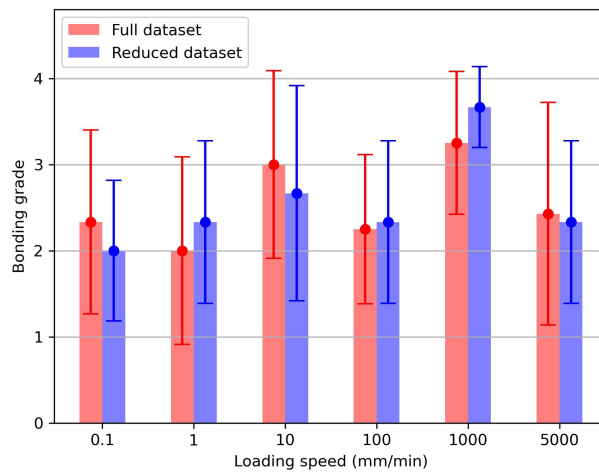
228 From the UTM, values of the measured load and of the prescribed displace-
229 ment were obtained. A characteristic load-displacement diagram is shown in
230 Figure 4a. The diagram can be separated into three characteristic branches.

231 The first ascending branch can be in turn divided into an initial linear-
232 elastic part and a nonlinear part due to the onset of damage in the adhesive.
233 The very first part of this ascending branch, which is slightly nonlinear due to
234 the initial settlement, was excluded from the analysis, as recommended by the
235 ASTM standard [5], and below 3 kN replaced by the best linear fit of the 2 to
236 3 kN data range. The load-displacement curve was then shifted horizontally
237 so that its first point is located at the origin of the coordinate system. The
238 difference between the raw and the corrected data in the first branch can be
239 seen by comparing the blue curves in Figures 4a and 4b, respectively.

240 The transition from the first to the second branch, characterised by a local
241 maximum, corresponds to further development of the damage process zone.
242 Within the second branch of the curve (red curves in Figures 4a and 4b) where



(a)



(b)

Figure 3: Mean values of a) bondline thickness and b) bonding grade for each of the loading-speed groups, for both full and reduced dataset are shown. Error bars mark \pm one standard deviation from the mean value.

243 the load decreases, the process zone fully develops and then crack propagation
244 starts, which can be either stable, as is the case of the tests considered here,
245 or unstable (dynamic) [26]. The third branch (green curves in Figures 4a and
246 4b) corresponds to a slowdown in crack propagation and an ascending load-
247 displacement curve. At the end of each test, the specimens were unloaded, but
248 this part of the load-displacement curve was omitted from the further analysis.

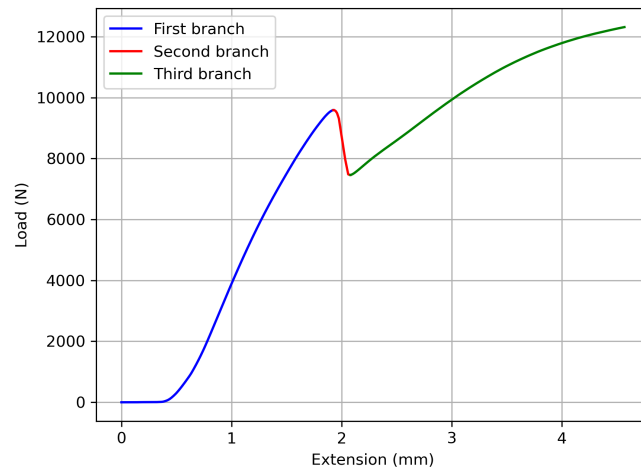
249 The UTM compliance was measured by loading a rigid steel block in three-
250 point bending. The determined value, which was $3.52 * 10^{-5}$ mm/N, was
251 then used to correct the measured displacements in the ENF load-displacement
252 curves.

253 The results for specimens tested at 5000 mm/min differ from other data
254 due to dynamic oscillations in the third branch, as shown by the green dashed
255 line in Figure 4b. 5000 mm/min data were acquired with a sampling rate of 5
256 kHz. To obtain a curve shape consistent with those observed at other loading
257 speeds, the third branch was filtered using the Savitzky-Golay convolution [27]
258 with an 81 data-point window and a second order polynomial. By doing this,
259 the underlying shape of the load-displacement diagram in the third branch was
260 obtained (solid green line in Figure 4b). Finally, a part of the second branch
261 below the intersection with the filtered third branch was discarded (dashed red
262 curve in Figure 4b).

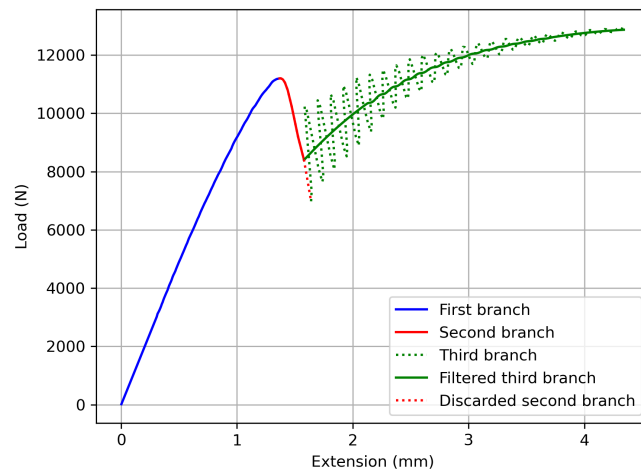
263 In summary, the raw data from the UTM were corrected by replacing the
264 initial non-linearities with linear data, accounting for rig compliance and, if
265 necessary, removing the inertial effects by filtering the third branch.

266 3. Construction of average parametrised load-displacement curves

267 If load-displacement curves of four tests performed at 1 mm/min are com-
268 pared (see grey curves in Figure 5), it can be noticed that the scatter is most
269 pronounced in the middle part (around the second branch) of the curve and is
270 defined not only by a vertical, but also by a horizontal offset. To fully assess
271 the rate-dependent behaviour of the adhesive in mode II in terms of the load-



(a) 10-2 specimen



(b) 5000-3 specimen

Figure 4: Two representative load-displacement curves with three characteristic branches for specimens tested at a) 10 mm/min (representative for the range of speeds from 0.1 to 100 mm/min) and b) 5000 mm/min.

272 displacement response, this scatter needs to be accounted for by averaging the
 273 load-displacement curves for each loading speed and by quantifying the vari-
 274 ation of results around the average response. However, computing the mean
 275 value of the curves with respect to displacements, as classically done for most
 276 cases, e.g. for the DCB test [13], results in a non-physical curve (see the blue
 277 curve in Figure 5), which does not represent the characteristic behaviour during
 278 the ENF test with three distinctive branches. In particular, the characteristic
 279 load drop that follows the peak (the second branch), used for determining the
 280 fracture resistance in mode II, is completely lost by using such an averaging
 281 method.

282 To best of the author's knowledge, the problem of how to construct the av-
 283 erage load-displacement curve for a given experimental ENF test dataset has
 284 not been raised. Knowing the shape of the average load-displacement curve
 285 for a given experimental dataset offers the possibility of analysing the rate-
 286 dependent behaviour of adhesive joints in a more rigorous and comprehensive
 287 way, as explained later in more detail. Furthermore, such average curves signifi-
 288 cantly improve and facilitate the calibration of numerical models for simulating
 289 adhesive debonding, as well as the assessment of their predictive capabilities.
 290 Motivated by this, a novel method for the calculation of an average ENF load-
 291 displacement curve, based on the curve parametrisation, is presented in the rest
 292 of this section.

293 *3.1. Fitting procedure for the experimental data*

294 As explained in the last section, the experimentally obtained load-displacement
 295 curve can be separated in three characteristic branches, connected by two smooth
 296 transitions. The three branches can be approximated by three non-linear func-
 297 tions, which we will refer to as branch functions, that intersect in proximity of
 298 local maximum and minimum values in the load-displacement curve. The linear
 299 least squares method was used to fit the three branch functions.

300 The first ascending branch is fitted with a quadratic function

$$f_1(x) = (a_{11} + a_{12}x) x, \quad (1)$$

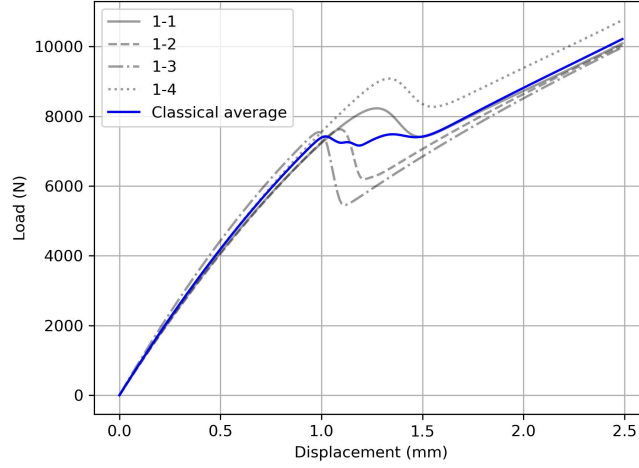


Figure 5: Load-displacement curves for specimens tested at 1 mm/min. The classical averaging method by taking the mean value of the load for each displacement produces the blue curve, which is non-representative of the physics of the ENF test.

301 where a_{11} and a_{12} are unknown constant parameters determined by the fitting
 302 procedure.

303 The analytical LEFM solution for the second descending branch in an ENF
 304 test (before the crack tip reaches the load application point) is [28]

$$v(F) = \frac{FL^3}{48EI} + \frac{(64G_{II,c}bEI)^{3/2}}{\sqrt{3}F^2}, \quad (2)$$

305 but for the presented procedure an inverse function $F(v)$ is needed. To this
 306 end, the following third order negative power function was found to be the most
 307 suitable:

$$f_2(x) = a_{21}x^{-1} + a_{22}x^{-2} + a_{23}x^{-3}, \quad (3)$$

308 while the third ascending branch is fitted with the following cubic function:

$$f_3(x) = (a_{31} + (a_{32} + a_{33}x) x) x, \quad (4)$$

309 where a_{ij} ($i = 2, 3$ and $j = 1, 2, 3$) are unknown constant parameters determined
 310 by the fitting procedure. While the choice of the fitting function for the second

311 branch is based on the analytical solution of the ENF test, it is worth noting
 312 that for the remaining two branches the polynomial expressions have been cho-
 313 sen based on a purely phenomenological approach, but they do reproduce the
 314 experimental response with good accuracy.

315 Functions $f_1(x)$, $f_2(x)$ and $f_3(x)$ are defined on the entire domain (for any
 316 $x \geq 0$). In this way, as shown in Figure 6, they can be used to create a continuous
 317 function that captures the whole load-displacement diagram as

$$F(x) = f_1(x)w_1(x) + f_2(x)w_2(x) + f_3(x)w_3(x), \quad (5)$$

318 with

$$\begin{aligned} w_1(x) &= 1 - S_1(x), \\ w_3(x) &= S_2(x), \\ w_2(x) &= 1 - w_1(x) - w_3(x) = S_1(x) - S_2(x), \end{aligned} \quad (6)$$

319 acting as weight functions that manage the transition between the three branches
 320 (see Figure 7a) based on a sigmoidal logistic function

$$S_i(x) = \frac{1}{1 + \exp(-k_i(x - \mu_i))}, \quad (7)$$

321 with $i = 1, 2$, which takes a value from the interval $< 0, 1 >$. In Equation
 322 (7), parameters μ_i define the x -coordinates at which the logistic function takes
 323 value of 0.5, while parameters k_i govern the rate of the transition between the
 324 branches (see Figure 7). Smaller values of k_i result in a smoother transition
 325 between the branches, while larger values result in a rapid transition. Note
 326 that k_i must be positive to ensure that the logistic function is monotonically
 327 increasing with x (as shown in Figure 7b).

328 The second function, used to fit the second branch, tends to infinity (either
 329 positive or negative, depending on the parameters) as x approaches zero. If
 330 the weight function w_2 has a small, but non-zero value in this region, a global
 331 function from Equation (5) will take a value significantly different from 0 at
 332 $x = 0$. For this reason a correction of the second function is made. Since the
 333 second function does not play an important role before the local maximum, the

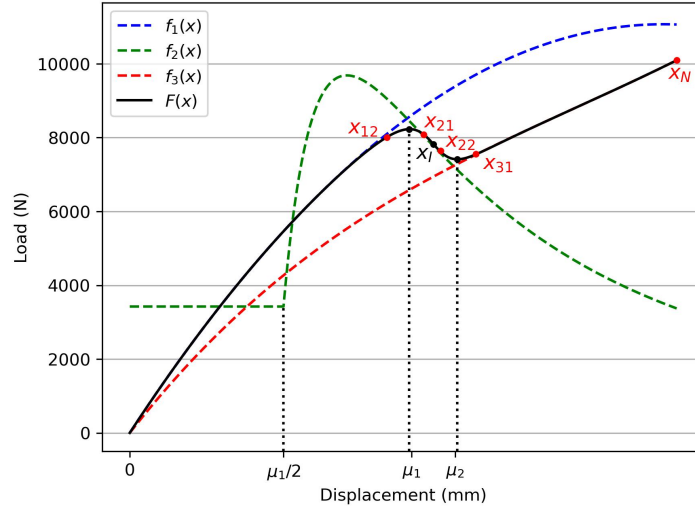


Figure 6: Schematic of the parametrised curve $F(x)$ obtained as a weighted combination of branch functions $f_i(x)$, $i = 1, 2, 3$, with the characteristic limit points (marked in red).

334 value of x used in the function is replaced by the value

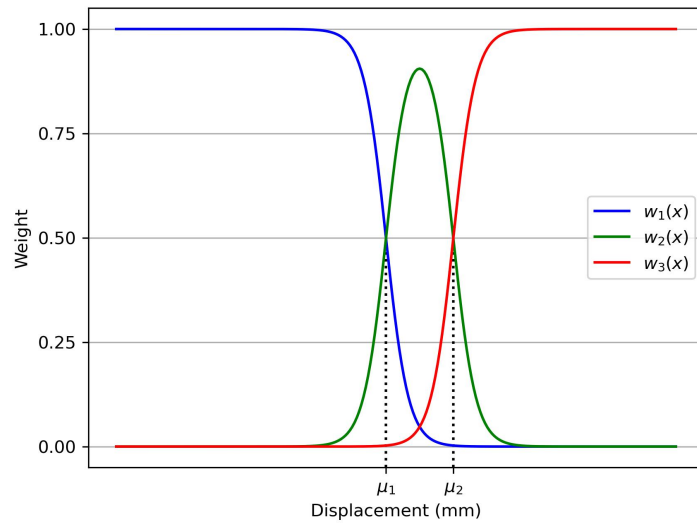
$$\bar{x} = \begin{cases} x_w & \text{for } x < x_w \\ x & \text{for } x \geq x_w. \end{cases} \quad (8)$$

335 where it has been set $x_w = \mu_1/2$, see Figure 6.

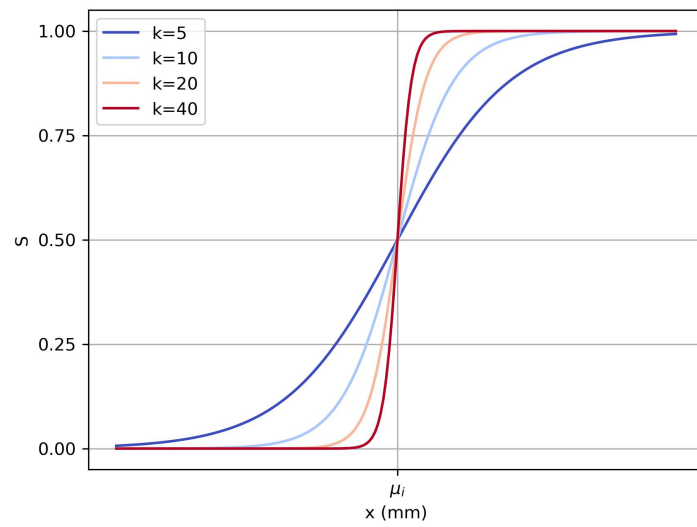
336 In order to fit the load-displacement curve using Equation (5), 12 parameters
 337 in total are needed: eight parameters for the branch functions and four param-
 338 eters for the transition functions. A novel curve-parametrisation algorithm was
 339 developed for this task, with its flowchart shown in Figure 9. The procedure
 340 consists of three steps: curve segmentation, curve fitting on individual segments
 341 and curve fitting on the transition region.

342 3.1.1. Step 1: curve segmentation.

343 In this first step, the load-displacement data, corrected in the way explained
 344 above, is imported. The numerical first derivative of the load-displacement curve
 345 is approximated by the 2-point central difference method, and its minimal value,
 346 corresponding to the curve inflection point (x_I, F_I) , is located. Using this point,



(a)



(b)

Figure 7: Plot of: a) weight functions $w_i(x)$ that define the transition between the branch functions $f_i(x)$, $i = 1, 2, 3$, b) a sensitivity analysis of logistic transition functions $S_i(x)$, $i = 1, 2$.

347 which falls within the second branch, approximately dividing it in the middle,
 348 the load-displacement curve is split into two parts. The maximum load value
 349 in the data before the inflection point corresponds to the local maximum point
 350 (x_M, F_M) , whereas the minimum load value in the data after the inflection
 351 point corresponds to the local minimum point (x_m, F_m) .

352 In order to obtain a good fit of the three characteristic branches, two tran-
 353 sition regions between them need to be suitably determined and then discarded
 354 from the piecewise fitting of each branch. The limiting points of the domains on
 355 which the first and third branches are fitted (see Figure 6) are calculated using
 356 the x -coordinates of previously determined local extrema values as

$$\begin{aligned} x_{12} &= x_M - (x_I - x_M) = 2x_M - x_I \\ x_{31} &= x_m + (x_m - x_I) = 2x_m - x_I, \end{aligned} \quad (9)$$

357 essentially mirroring the distance between the local extrema points and the slope
 358 inflexion point about the local extrema.

359 For the specimens tested at a speed of 5000 mm/min, due to third branch
 360 filtering, the minimum point of the second branch slope F_I is not located close
 361 to the middle of the branch. Therefore, for these specimens, x_I in Equation (9)
 362 is replaced by $0.5(x_m - x_M)$ to compute x_{12} and x_{31} .

363 Having determined x_{12} and x_{31} in this way, the fitting domains for the first
 364 and third branches are set as $[0, x_{12}]$ and $[x_{31}, x_N]$, respectively, where x_N is
 365 the x -coordinate of the last data point (see Figure 6).

366 3.1.2. Step 2: curve fitting on the individual segments.

367 Using the fitting domains defined in the previous step, in this second step,
 368 the linear least squares method is applied to fit the first and third branches.
 369 Fitting the first branch using Equation (1) and third branch using Equation (4)
 370 result in the determination of the five fitting parameters $a_{11}, a_{12}, a_{31}, a_{32}, a_{33}$.

371 To complete the piecewise fitting, the domain $[x_{21}, x_{22}]$ for fitting the second
 372 branch using Equation (3), whose corresponding codomain is $[F_{22}, F_{21}]$ (see
 373 Figure 8), needs to be defined. The codomain size is defined as a fraction p_F of

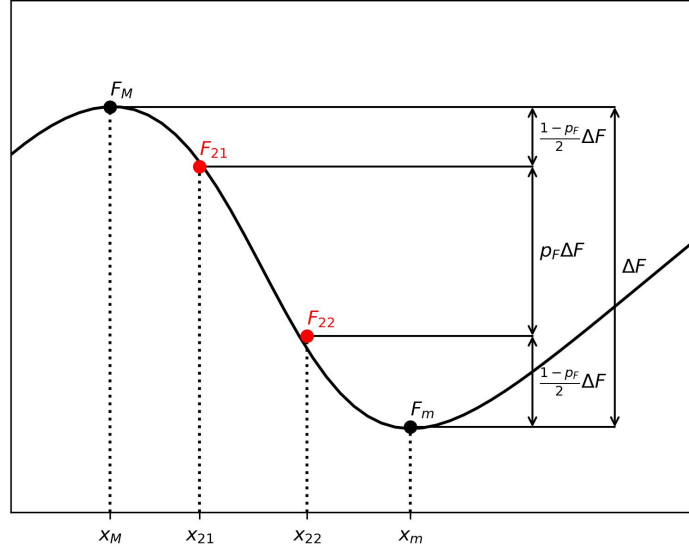


Figure 8: Schematic representation of second branch fitting domain limits x_{21} and x_{22}

374 the force drop in the second branch $\Delta F = F_M - F_m$, with $0 < p_F < 1$, so that
 375 $F_{22} - F_{21} = p_F \Delta F$. Therefore, F_{21} and F_{22} are given by:

$$\begin{aligned} F_{21} &= F_M - \frac{1-p_F}{2} \Delta F \\ F_{22} &= F_m + \frac{1-p_F}{2} \Delta F. \end{aligned} \quad (10)$$

376 The x -coordinates corresponding to F_{2i} define x_{2i} , with $i = 1, 2$, and are the
 377 limits of the second branch fitting domain. These points are shown in Figure 8.

378 A decrease in parameter p_F results in a smaller fitting domain and a larger
 379 distance of its limits from the extrema points. As Equation (3) needs to have at
 380 least three points in order to fit the second branch, for specimens with a small
 381 number of points (two or less) in the second domain, an additional one point is
 382 added on either side of the domain.

383 The second branch is then fitted using Equation (3) across domain $[x_{12}, x_{21}]$
 384 and the three additional parameters a_{21} , a_{22} and a_{23} are determined. At the
 385 end of step 2, branch functions $f_1(x)$, $f_2(x)$ and $f_3(x)$ are fully defined.

386 *3.1.3. Step 3: curve fitting on the transition region.*

387 Global fitting using Equation (5) is performed in this step. For this non-
 388 linear fit, a Limited-memory Broyden–Fletcher–Goldfarb–Shanno with Bounds
 389 (L-BFGS-B) non-linear optimisation algorithm [29] is used for the mean squared
 390 error (MSE) minimisation. This algorithm, which falls into the broader category
 391 of the quasi-Newton methods, is chosen because it offers a simple way to impose
 392 boundaries on the search domains of the fitting parameters, thus ensuring a
 393 convergence to a correct fit. The global fitting is performed on the domain
 394 $x \in [x_{12}, x_{31}]$ only, which means that the first and third branch parameters
 395 determined in step 2 remain constant. This allows for a smoother convergence,
 396 while the accuracy of the fit is not compromised as typically the R^2 of these
 397 branches on their respective domains is in the 0.99+ range.

398 The parameters to be optimised are those defining the second branch (a_{21} ,
 399 a_{22} , a_{23}) and the transition parameters from Equation (7), namely μ_1 , μ_2 , k_1 , k_2 .
 400 For these 7 parameters, initial values need to be provided. For the second branch
 401 parameters, the initial values are those obtained in Step 2. The x -coordinates
 402 of the local extrema, x_M and x_m , are taken as initial values of parameters μ_1
 403 and μ_2 , respectively.

404 For the initial values of parameters k_i , from Equation (7) we can derive the
 405 term for the rate of change of the logistic function

$$k_i = -\frac{\ln\left(\frac{1}{S_i(x)} - 1\right)}{x - \mu_i}, \quad (11)$$

406 where $x - \mu_i$ is the length on which the logistic function changes from 0.5 to
 407 $S_i(x)$. Note that function $S_i(x)$ has two asymptotes that take the values of 0
 408 and 1, with an infinitely long transition between them (see Figure 7b). In order
 409 to initialise k_i with a reasonable value, we set limit values of function $S_i(x)$ for
 410 which the transition between those limits takes place over a finite length. As
 411 function $S_i(x)$ is symmetric with respect to μ_i , only the upper limit values is
 412 set to 0.95, as 1 is not acceptable. Therefore, we need to define a value \hat{x}_i of x
 413 for which $S_i(\hat{x}_i) = 0.95$.

414 Defining $\hat{x}_1 = \mu_1 + x_I - x_{12}$ and $\hat{x}_2 = \mu_2 + x_{31} - x_I$, and replacing these
 415 two values into Equation (11) has been shown to provide values of k_1 and k_2 ,
 416 respectively, that lead to a stable fitting procedure and provide satisfactory
 417 accuracy of the fit.

418 Next, to ensure the convergence of the iterative procedure, boundaries on
 419 the search domain of the transition parameters must be set. The L-BFGS-B
 420 optimisation algorithm was chosen for its ability to set such boundaries, which
 421 in turn stabilises the fitting procedure. For the parameters μ_i , the domains
 422 are defined as $\mu_1 \in [x_{12}, x_{22}]$ and $\mu_2 \in [x_{21}, x_{31}]$. The domains on the rate
 423 of transition are set up to be $k_i \in [0, 100]$ for $i = 1, 2$, with the larger value
 424 chosen arbitrarily to ensure consistency of the parameters inside the loading-
 425 speed groups.

426 After the computation of the initial values and the ranges of their possible
 427 variations, global fitting is performed, resulting in new values a_{21} , a_{22} , a_{23} ,
 428 μ_1 , μ_2 , k_1 and k_2 . Using Equation (5) and the parameters of the first and
 429 third branch functions (which did not change), a fit of the experimental data is
 430 constructed. As the value of R^2 generally takes a value of 0.99+ for the entire
 431 domain and a value of 0.97+ for the fitting domain $[x_{12}, x_{31}]$, the accuracy of
 432 the fit must be visually evaluated. In order to achieve a better fit, parameter
 433 p_F can be reduced and the procedure is repeated from the local fitting of the
 434 second branch function onward (see Figure 9). New initial values for the second
 435 branch parameters are calculated and all other parameters, including initial
 436 values and search domain boundaries, remain unchanged. In this study a value
 437 of $p_F = 0.95$ was found to be appropriate for most specimens, with a reduction
 438 down to $p_F = 0.85$ for few specimens (0.1-3, 5000-2 and 5000-6).

439 3.1.4. Results of the fitting procedures

440 The representative load-displacement curves fitted from the experimental
 441 data using the procedure described above are shown in Figure 10. A variety of
 442 different load-displacement responses are presented to illustrate the robustness
 443 of the method. It can be seen that specimens 10-3 and 100-1 had a very fast

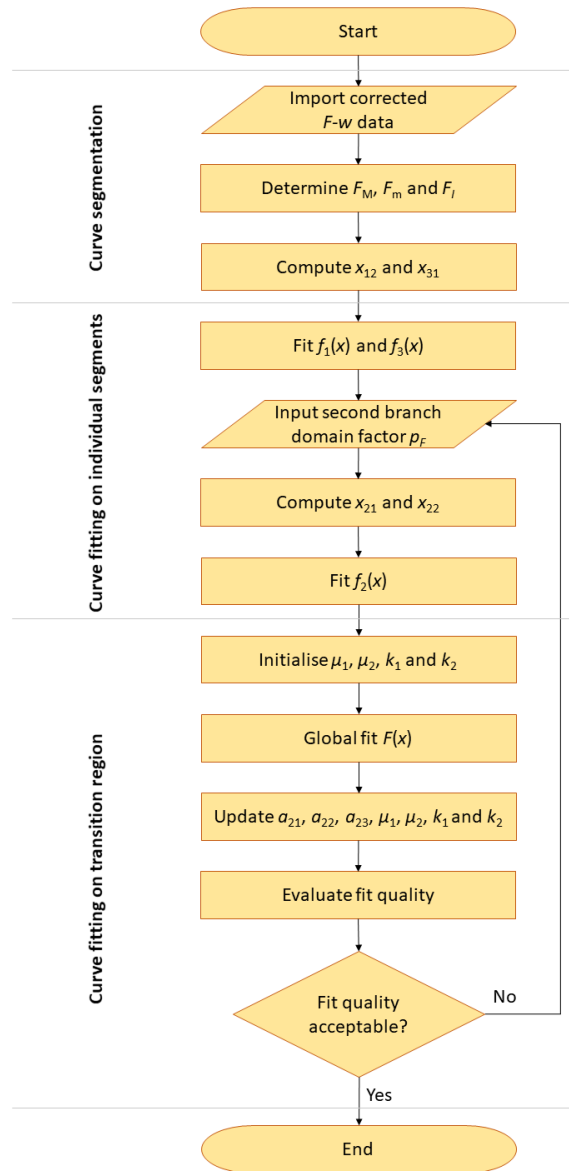


Figure 9: Flowchart of the algorithm used for curve fitting of the experimental load-displacement data.

444 initial crack propagation, which led to a lower number of data-points recorded
445 in the second branch. Even in such circumstances, which also appeared for
446 other specimens tested at different speed, the proposed procedure was able
447 to produce a robust and accurate fit. For specimens 100-1, 1000-2 and 5000-3
448 (amongst others), a change in the third branch, due to yielding of the aluminium
449 adherends can be seen. On all 100 mm/min specimens, a specific bump was
450 noticed after the local minimum on all specimens, which made the fitting of this
451 part slightly less accurate.

452 3.2. Constructing the average load-displacement curves

453 A mean value of the parameters obtained by the fitting procedure from
454 the previous section for all specimens tested at the same loading speed can be
455 calculated. In this way we can construct the average ENF load-displacement
456 curves using the global fitting equation (5).

457 The whole procedure also allows us to perform a statistical analysis on the
458 parameters and quantify the scatter in the results. The statistical and rate-
459 dependence analysis of the calculated parameters is given in Appendix B.

460 Figure 11 shows the load-displacement curves of all ENF specimens alongside
461 their respective average curves. In this figure, specimens which were discarded
462 based on their large thickness are marked in orange and those discarded based
463 on their low bonding grade are marked in red. Referring to Table A.3, it can be
464 concluded that a low bonding grade reduces the peak load and initiates crack
465 propagation at lower displacement values, while increasing the bondline thick-
466 ness has the opposite effect. This is also consistent with the statistical analysis
467 of the fitting parameters presented in Appendix B, where it can be observed
468 that the parameters of the discarded specimens fall outside the error bars in
469 Figures B.16 and B.17. It can be noticed that parameters μ_i increase with the
470 bondline thickness, while smaller values of k_i indicate smoother transitions be-
471 tween branches and thus more ductile behaviour. Specimens discarded due to
472 their low bonding grade had the lowest values of μ_i in their respective groups,
473 while those discarded due to their thick bondlines showed the highest values of

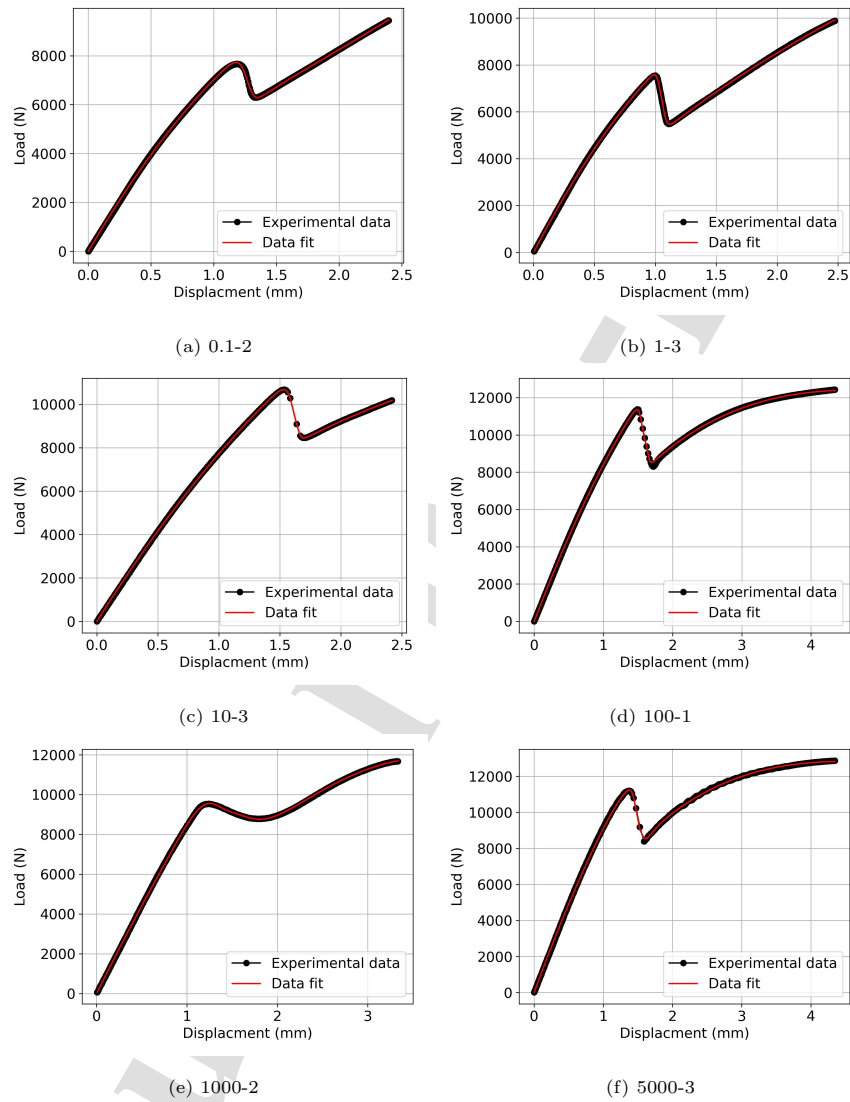


Figure 10: Comparison of representative experimental load-displacement curves with the corresponding fitted parametrised curves for each testing speed.

474 μ_i . This indicates that a parameter analysis following the curve-fitting proce-
475 dure can be used as a reliable tool for the quantitative identification of faulty
476 specimens.

477 The average curves, constructed with the mean values of the parameters in
478 Equation (5), are shown in blue. A distinction is made between the average
479 load-displacement curves constructed using the mean values of the parameters
480 from the full and reduced datasets (3 specimens). It can be seen how discarding
481 certain specimens changes the average curves.

482 It is obvious that all 1000 mm/min curves have a different shape than the
483 curves loaded at different speeds. In particular, the characteristic shape of the
484 second branch with a sudden load drop is almost completely lost. However,
485 comparing the 1000 mm/min curves with the 100 and (filtered) 5000 mm/min
486 curves reveals that such a behaviour cannot be attributed to the rate-dependent
487 behaviour of the adhesive. Note that the average load-displacement curves for
488 100 and 5000 mm/min are very similar in shape and values, which indicates
489 that the rate-dependent effects could be very limited in that range of speeds.
490 In addition, the first branch, the peak and the third branch in the average
491 load-displacement curves across 100, 1000 and 5000 mm/min are also very
492 close to each other. Therefore, it is very likely that the 1000 mm/min load-
493 displacement curves were affected by the machine load-cell responsiveness and
494 data-acquisition system. Investigating the origin of this issue is outside the
495 scope of this work. Nevertheless, because the first and third branch of the 1000
496 mm/min load-displacement curves are unaffected by this, these curves are still
497 included in further analyses.

498 The average load-displacement curves for all loading speeds determined from
499 the full and reduced datasets as explained above are shown in Figure 12. It can
500 be seen that the reduced dataset shows rate-dependent effects in a clearer and
501 more regular way than the full dataset. Rate-dependent effects in the reduced
502 dataset manifest in the following ways:

- 503 1. The initial stiffness increases with increasing loading speed.

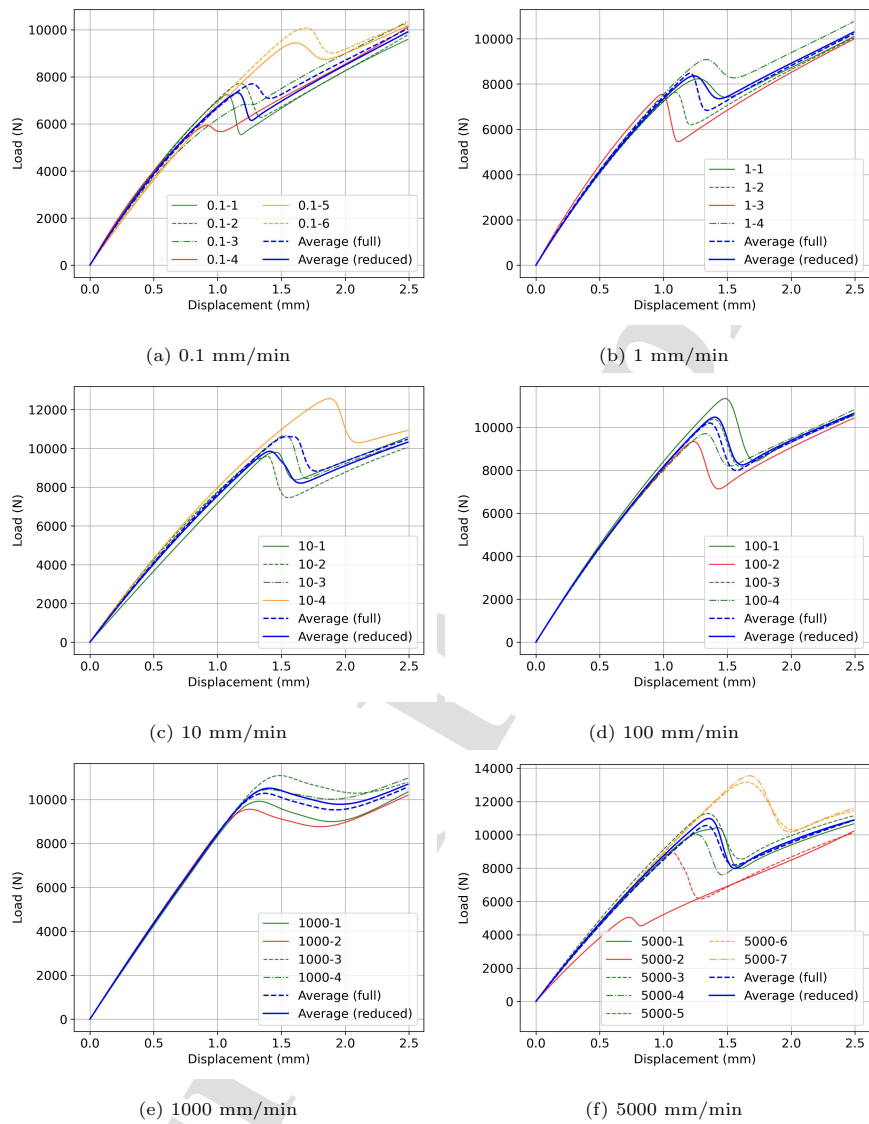


Figure 11: Individual parametrised load-displacement curves fitted from the experimental data with the corresponding parametrised average curves for each testing speed. Specimens from the reduced dataset are marked in green, those excluded due to thick bondline are marked in orange, while those excluded based on their low bonding grade are marked in red. The average curves are marked in blue (solid for the reduced dataset and dashed for the full dataset).

- 504 2. The reduction in stiffness along the first branch becomes less pronounced
505 with increasing loading speed.
- 506 3. The peak force increases with increasing loading speed.
- 507 4. Both extrema (maximum and minimum) on the second branch occur at
508 larger displacement with an increase in loading speed up to 10 mm/min,
509 after which the trend changes.
- 510 5. Force drop becomes larger with an increase in loading speed.
- 511 6. With increasing loading speed, the third branch is shifted vertically, while
512 maintaining the same slope.

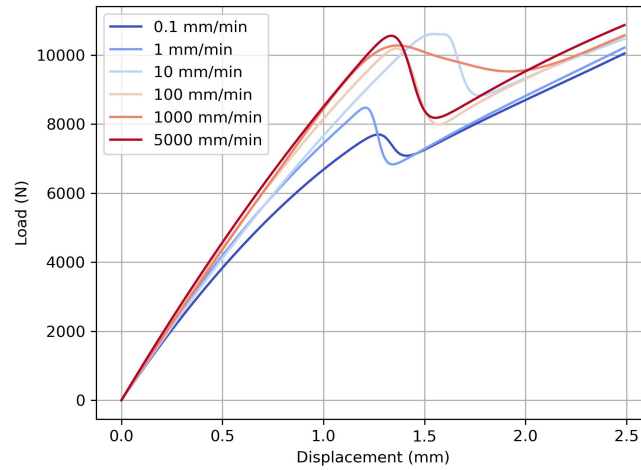
513 These insights into the rate-dependent behaviour in mode-II debonding would
514 not be possible without the evaluation of average load-displacement curves us-
515 ing the presented methodology (Figure 12). A similar approach could also be
516 applied to other debonding tests exhibiting significant scatter.

517 **4. Verification of the proposed method by critical energy release rate** 518 **comparison**

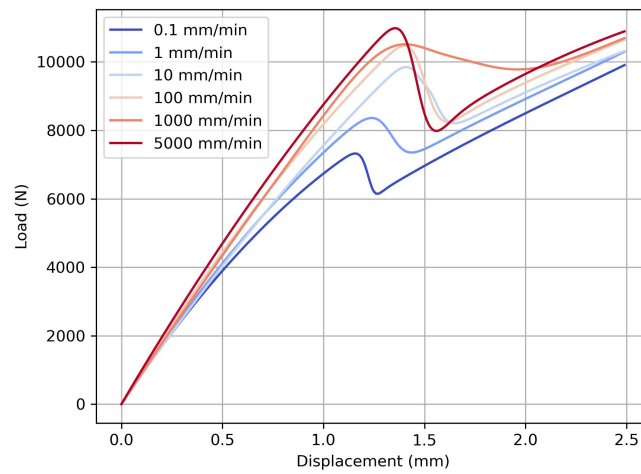
519 In this section, the accuracy of the proposed curve parametrisation method
520 is assessed by comparing the values of the critical energy release rate evaluated
521 using the constructed average load-displacement curves with those obtained by
522 the standard specimen-by-specimen procedure. In both cases, the well estab-
523 lished compliance-based beam method (CBBM) [3] was used to calculate the
524 critical energy release rate.

525 *4.1. Compliance-based beam method (CBBM)*

526 CBBM employs the equivalent-crack-length concept, thus avoiding the mea-
527 surement of the crack length, which, as discussed in more detail in the intro-
528 duction, can be quite challenging in ENF mode-II testing. The suitability and
529 accuracy of this method have previously been demonstrated for adhesive joints
530 bonded with the same adhesive studied in this paper (Araldite[®] 2015) [3].



(a)



(b)

Figure 12: Constructed average curves for all loading speeds: a) full dataset and b) reduced dataset.

531 Assuming a simply-supported two-layer beam, as depicted in Figure 1, with a
 532 crack length equal to a and a perfectly rigid connection along the bonded region,

533 the specimen's compliance during the test can be calculated using simple beam
534 theory accounting for shear effects [2] as

$$C = \frac{3a_e^3 + 2L_0^3}{8E_fbd^3} + \frac{3L_0}{10G_mbd}, \quad (12)$$

535 where E_f is the adherend flexural modulus calculated as

$$E_f = \frac{3a_0^3 + 2L_0^3}{8bd^3C_{0corr}}, \quad (13)$$

536 G_m is the shear modulus of the arms and a_e is the equivalent crack length which
537 accounts for the influence of the damage process zone so that

$$a_e = a + \Delta a_{DPZ} = \left(\frac{C_{corr}}{C_{0corr}} a_0^3 + \frac{2}{3} \left(\frac{C_{corr}}{C_{0corr}} - 1 \right) L_0^3 \right)^{1/3}. \quad (14)$$

538 In these expressions a_0 is the length of the initial crack (notch) and C_{corr} is the
539 measured compliance C_{msr} corrected for shear deformation

$$C_{corr} = C_{msr} - \frac{3L_0}{10G_mbd}. \quad (15)$$

540 Note that the measured compliance is determined from the load-displacement
541 data as the quotient of the displacement and load. The initial compliance C_0 is
542 taken as the compliance at the beginning of the test, which in this case is con-
543 stant due to the removal of the initial non-linearities from the load-displacement
544 diagram. C_{0corr} is the value of initial compliance, corrected using Equation (15).
545 Now, by using the Irwin-Kies equation

$$G_{II,c} = \frac{F^2}{2b} \frac{dC}{da}, \quad (16)$$

546 substituting C from Equation (12) and taking the derivative with respect to a_e
547 instead of a , the mode-II critical energy release rate is follows as

$$G_{II,c} = \frac{9F^2 a_e^2}{16b^2 d^3 E_f}. \quad (17)$$

548 The only material parameter required in the CBBM is the shear modulus
549 G_m , where, due to the limited influence on the critical energy release rate, the
550 typical value can be used [30]. The value used in this analysis is the nominal
551 value for Al 6082-T6 aluminium of $G_m = 26$ GPa.

552 *4.2. Verification results and discussion*

553 The resulting fracture-resistance curves (R-curves) calculated from the parametrised
554 average curves for the reduced dataset are shown in Figure 13. Energy release
555 rate and equivalent crack length values were calculated for 0.1 mm displace-
556 ment increments. The common method to calculate $G_{II,c}$ from these curves is
557 to determine the mean value of the fracture resistance on the plateau. In this
558 study, the plateau was defined by points where the absolute value of the gradi-
559 ent of the R-curve, calculated using the 2-point central finite difference method,
560 does not exceed 0.1 N/mm^2 . Points that satisfy this condition are marked in
561 blue in Figure 13. It can be seen that at 1000 mm/min, the R-curve increases
562 monotonically instead of exhibiting the characteristic plateau, which is likely
563 a consequence of the previously discussed differences in the load-displacement
564 response.

565 The R-curves can also be computed for each individual specimen using their
566 respective load-displacement curves. The representative value of the critical
567 energy release rate is then obtained by calculating the mean of all values that
568 make up the plateau in the R-curve, which will be indicated here as 'standard
569 mean'. These values are reported in Table A.3 in Appendix A. The resulting
570 values of $G_{II,c}$ for all specimens are shown in Figure 14 for both the full and
571 the reduced dataset. For each loading speed, the standard mean of $G_{II,c}$ is
572 indicated in Figure 14 by black markers. As expected, by reducing the dataset,
573 the scatter of the computed values of $G_{II,c}$ is reduced for each speed. The values
574 of $G_{II,c}$ computed from the parametrised average load-displacement curves for
575 each loading speed are indicated in Figure 14 by dark blue markers.

576 Table 2 shows the values of $G_{II,c}$ calculated using the standard mean and
577 the presented curve-parametrisation averaging method, for both the full and the
578 reduced dataset. It can be seen that the agreement between the two approaches
579 is very good, with the maximum relative error less than 5.5%. The proposed
580 method yields larger values of $G_{II,c}$ than the standard mean in all cases except
581 for the slowest speed in the full dataset.

582 The standard deviations calculated along with the standard mean are also

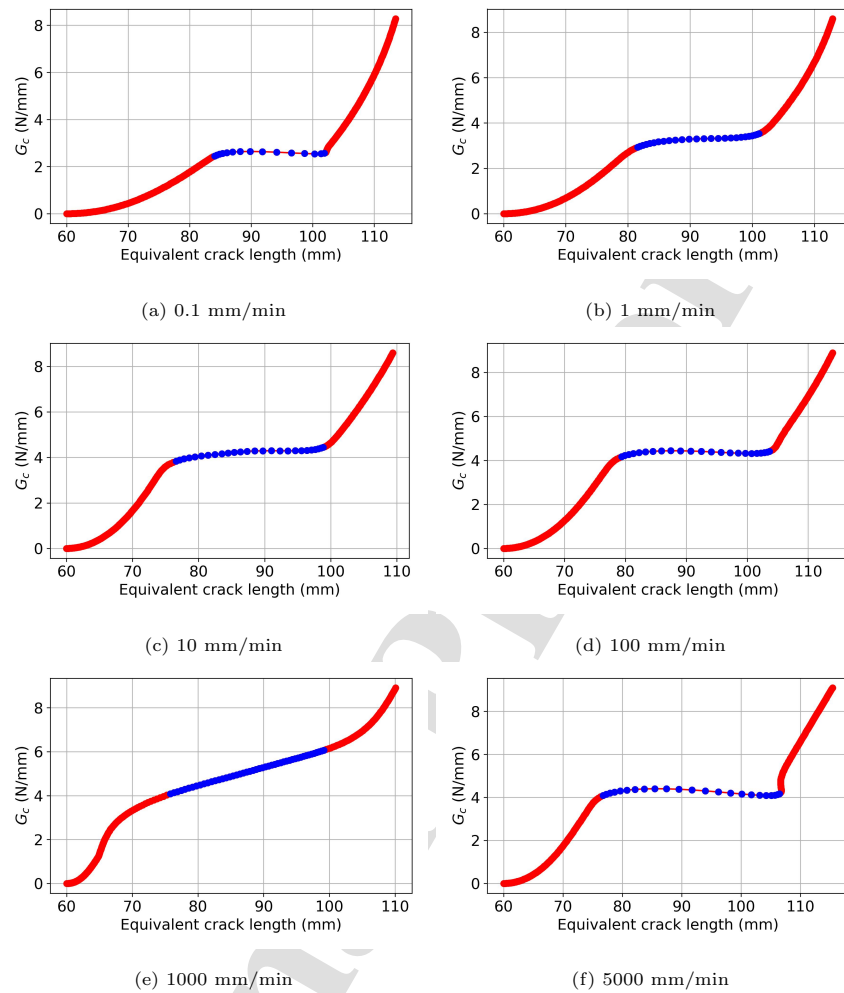
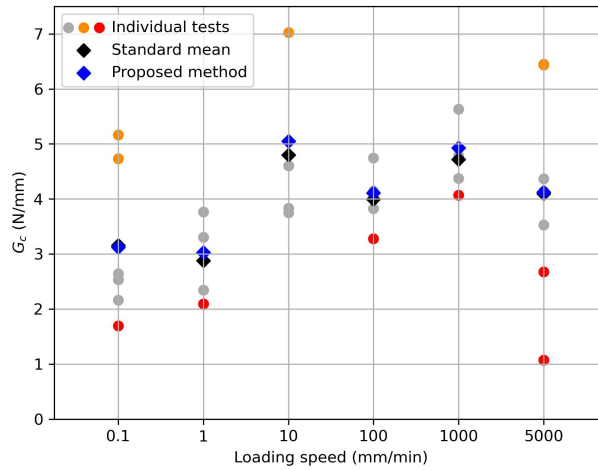


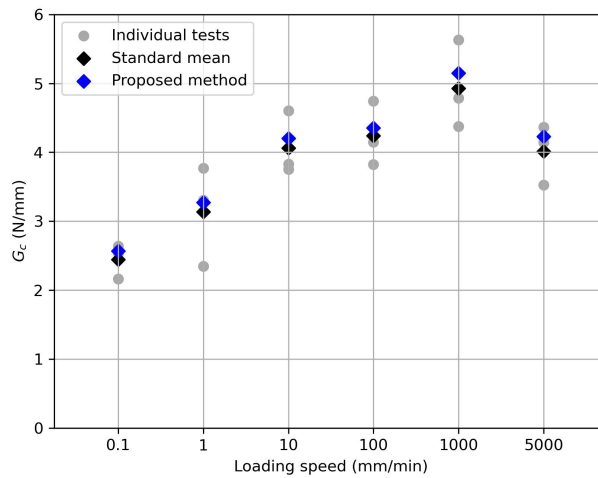
Figure 13: R-curves calculated using the load-displacement curves obtained by the novel curve parametrisation averaging method. These curves are calculated from the reduced dataset using the CBBM data-reduction scheme.

583 reported in Table 2. As expected, the standard deviation values decreased
 584 considerably for most loading speeds by reducing the dataset.

585 This comparison confirms that the proposed method for determining the
 586 parametrised average load-displacement curves is very accurate and reliable. Its
 587 ability to capture the global behaviour during crack propagation for an average



(a)



(b)

Figure 14: Comparison of critical energy rates obtained from experimental data and from the presented curve parametrisation averaging method: a) full dataset and b) reduced dataset. For the full dataset specimens discarded for their bondline thickness are marked orange and those discarded for their low bonding grade are marked red. Note that the two highest values for 5000 mm/min overlap.

Full dataset				
Loading speed (mm/min)	Standard mean (N/mm)	Standard deviation (N/mm)	Proposed method (N/mm)	Relative error (%)
0.1	3.155	1.309	3.121	-1.071
1	2.878	0.683	3.026	5.171
10	4.802	1.324	5.052	5.200
100	3.998	0.531	4.107	2.711
1000	4.716	0.585	4.929	4.533
5000	4.096	1.797	4.123	0.651
Reduced dataset				
Loading speed (mm/min)	Standard mean (N/mm)	Standard deviation (N/mm)	Proposed method (N/mm)	Relative error (%)
0.1	2.446	0.204	2.570	5.057
1	3.138	0.592	3.269	4.173
10	4.062	0.385	4.204	3.496
100	4.239	0.380	4.353	2.694
1000	4.930	0.522	5.152	4.495
5000	4.013	0.355	4.230	5.418

Table 2: Average values of $G_{II,c}$, calculated as standard mean and using presented curve parametrisation averaging method for full and reduced datasets.

588 specimen demonstrates that the complete curve, composed of three character-
589 istic branches, faithfully represents the average response of a group of ENF
590 specimens. To the best of the authors' knowledge, no method for constructing
591 such a representative average load–displacement curve for a set of ENF tests
592 has been proposed.

593 The results presented in Table 2 indicate a strongly rate-dependent be-
594 haviour of the adhesive, with significant increase in the fracture resistance for

595 the reduced dataset from approximately 2.5 N/mm at 0.1 mm/min to values
596 of about 4 N/mm at 5000 mm/min (not considering the higher value of about
597 5 N/mm at 1000 mm/min for the reasons that will be discussed later). In an
598 analogous analysis of the mode-I rate-dependent behaviour of DCB specimens
599 with the same adhesive and adherend material, an increase in mode-I fracture
600 resistance was reported from approximately 0.25 to 0.55 N/mm for the same
601 range of loading speeds [13]. As expected, the mode-II fracture resistance is
602 much higher than that in mode-I, which can be attributed to the contribution
603 of the effects of asperity and friction on the crack surfaces in compression [31].

604 To better assess the mode-II rate dependence of the tested adhesive, the
605 change in fracture resistance with loading speed, using values of $G_{II,c}$ obtained
606 using both methods and for both datasets, is shown in Figure 15. It can be
607 observed that reducing the dataset resulted in a more obvious trend in the rate-
608 dependent behaviour of the adhesive, in which the critical energy release rate
609 increases with the loading speed up to 1000 mm/min and then drops at 5000
610 mm/min. Because in the reduced dataset there is more uniformity among the
611 specimens (in terms of the bonding grade and bondline thickness), it will be
612 assumed that it represents the rate-dependent properties of the adhesive more
613 accurately than the full dataset.

614 However, the apparent maximum of $G_{II,c}$ at 1000 mm/min should not be
615 considered representative for the following reason. As explained earlier, in 1000
616 mm/min load-displacement curves (including the parametrised average curve)
617 the characteristic force drop after the peak is smoothed out (Figure 11e) due to
618 machine-induced interference in the measured response. As a result of this, the
619 1000 mm/min R-curves miss the characteristic plateau (Figure 13e), which in
620 turn results in a higher mean value of the critical energy release rate. There-
621 fore, by comparing the parametrised average load-displacement curves (Figure
622 12b) and the corresponding R-curves (Figure 13), it seems reasonable to expect
623 that the rate-dependent effect in the range of loading speeds between 10 and
624 5000 mm/min could be very limited. Consequently, a plateau, rather than a
625 maximum at 1000 mm/min, could be expected in Figure 15 from 10 to 5000

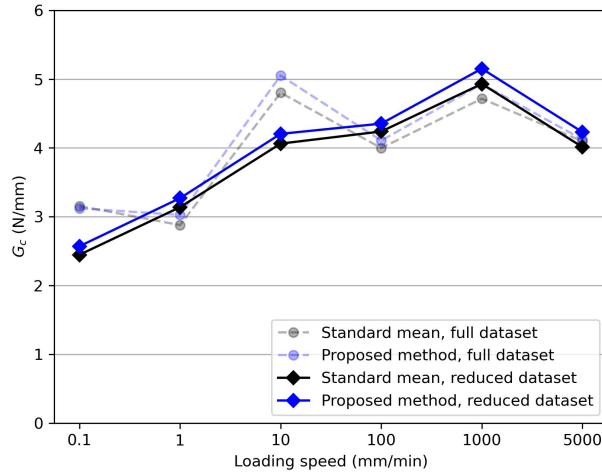


Figure 15: Average $G_{II,c}$ values calculated for full and reduced dataset, using classical method and method presented in this paper.

626 mm/min.

627 Although the previous discussion leads to the conclusion that $G_{II,c}$ reaches
 628 a plateau value of around 4 N/mm at 10 mm/min which remains approximately
 629 constant up to 5000 mm/min, there are also obvious rate-dependent effects in
 630 the first and third branches of the average load-displacement curves shown in
 631 Figure 12. However, these branches are not taken directly into account in the
 632 data-reduction schemes used to determine the fracture resistance of the adhe-
 633 sive. The proposed curve parametrisation method allows for comparison of
 634 the rate-dependence across the entire domain of the average load-displacement
 635 curves. In this way, a more comprehensive rate-dependent analysis of the adhe-
 636 sive debonding can be performed, accounting for the increase of both the initial
 637 stiffness in the first branch and the post-fracture load-bearing capacity in the
 638 third branch.

639 5. Conclusion

640 In this work, a novel methodology was developed for assessing the rate-
641 dependent behaviour of mode-II adhesive debonding using the ENF test. The
642 experimental load-displacement data were analysed using a novel automatic
643 curve-parametrisation method that can be easily employed to construct repre-
644 sentative average curves using the mean values of the fitting parameters. The
645 accuracy of the method was successfully verified by comparing the values of
646 the critical energy release rate for each loading-speed group computed from the
647 average parametrised load-displacement curves with those obtained using the
648 standard specimen-to-specimen analysis.

649 The presented method has been applied to study the rate dependence of
650 adhesive joints made of aluminium arms bonded with Araldite[®] 2015 adhe-
651 sive tested at six different loading speeds ranging from 0.1 to 5000 mm/min.
652 Using the standard approach for assessing the mode-II rate-dependent fracture
653 resistance, $G_{II,c}$ was found to increase from approximately 2.5 N/mm at 0.1
654 mm/min to 4.2 N/mm at approximately 10 mm/min, after which it reaches
655 a plateau. However, the parametrised average load-displacement curves con-
656 structed for each loading speed indicated that the rate-dependent effects have
657 a monotonically increasing trend in parts of the load-displacement curves that
658 were not considered for evaluation of $G_{II,c}$. In particular, the initial stiffness,
659 peak load and post-peak bearing capacity showed an increase with increasing
660 the loading speed.

661 The proposed procedure to determine average load-displacement curves for
662 ENF tests, for which to the best of the authors' knowledge no other method
663 had previously been proposed in the literature, offers several benefits when
664 compared to the standard procedure of fracture characterisation based solely
665 on the evaluation of the critical energy release rate. In particular:

- 666 1. The parametric representation of the average load-displacement curves
667 enables a robust quantitative analysis of the scatter in the underlying
668 data, which in turn can be used for automatic detection of specimens that

- 669 deviate from the representative response.
- 670 2. The average load-displacement curves can be used as an efficient tool for a
671 comprehensive qualitative and quantitative analysis of the rate-dependent
672 behaviour. In particular, rate-dependent effects can also be assessed on
673 the first and third branch of the load-displacement curve, which, as con-
674 firmed by the presented analysis, can reveal important information that is
675 not available in case of the standard assessment of the mode-II fracture re-
676 sistance. Moreover, the rate dependence can be studied at the parameter
677 level (as illustrated in Figure B.18).
- 678 3. For numerical simulations based on nonlinear models whose input param-
679 eters are not limited to $G_{II,c}$, for example when cohesive-zone models
680 are used, the proposed method enables a more robust and accurate iden-
681 tification of the model parameters, as they allow a direct quantitative
682 assessment of the agreement between the simulation results and the rep-
683 resentative experimental response.
- 684 4. The determination of the average load-displacement curves also for third
685 branch and the transition between the second and third branch can be
686 particularly useful to evaluate the role of friction and for the parameter-
687 identification of models that account for frictional effects [31].

688 The high modularity of the presented method allows for its easy modifica-
689 tion, which can be employed for processing the results of different debonding
690 tests, including mode-I and mixed-mode tests, as well as other types of mode-II
691 tests, such as ELS, 4ENF and TENF. It is also worth noting that, while the
692 methodology presented in this article is clearly not predictive, it can be used to
693 calibrate advanced non-linear models which can indeed predict the response of
694 complex bonded components or assemblies used in engineering applications.

695 The results shown in this paper will be employed in future work that will
696 focus on the numerical simulations of the ENF tests using cohesive-zone models
697 that account for rate-dependence and frictional effects. Future work should also
698 include conducting similar tests within a wider range of loading speeds to fully

699 characterise its mode-II rate-dependence.

700 **CRedit authorship contribution statement**

701 **Damjan Jurković:** Methodology, Conceptualisation, Investigation, Soft-
702 ware, Validation, Formal analysis, Writing - Original Draft, Writing - Review
703 & Editing, Visualisation, Data curation.

704 **Leo Škec:** Methodology, Conceptualisation, Project Administration, Re-
705 sources, Funding acquisition, Writing - Review & Editing, Supervision.

706 **Giulio Alfano:** Methodology, Conceptualisation, Project Administration,
707 Resources, Funding acquisition, Writing - Review & Editing, Supervision.

708 **Data availability**

709 The data supporting the findings of this study and the Python code for the
710 curve-parametrisation-based curve fitting are openly available in the Reposi-
711 tories of the University of Rijeka, Faculty of Civil Engineering, and of Brunel
712 University of London at [link to be added after the paper is accepted].

713 **Funding**

714 This project has received funding from the European Union's Horizon 2020
715 research and innovation programme under the Marie Skłodowska-Curie grant
716 agreement No. 701032 (MOLAY-STRUDEL). In addition, this work has been
717 supported by the Croatian Science Foundation (HRZZ DOK-2021-02-6065) and
718 the European Union – NextGenerationEU through a contract between the Uni-
719 versity of Rijeka and the Ministry of Science, Education and Youth of the Re-
720 public of Croatia (PU-437 uniri-iz-25-288).

721 **Appendix A. Measured values for all specimens**

722 Table A.3 shows the measured values of bondline thickness, bonding grade
723 and $G_{II,c}$ for all specimens, the latter calculated using the CBBM and the mea-
724 sured data. The last column indicates whether the specimens were discarded

725 from the reduced dataset and specifies the reason for their exclusion (low bond-
726 ing grade or thick bondline).

727 **Appendix B. Parameter analysis**

728 To assess the variation of the fitting parameters from their respective mean,
729 the relative deviation from the mean was calculated for each specimen. This
730 was done for all specimens tested and the results are shown in Figures B.16 and
731 B.17, along with their relative standard deviation (RSD) error bars. As before,
732 specimens which were discarded based on their large thickness are marked in
733 orange and those discarded based on their low bonding grade are marked in red.

734 It can be seen that the largest scatter in the parameter values is generally
735 in the parameters defining the second branch of the load-displacement diagram
736 (specifically a_{21} and a_{23}). This is consistent with the scatter that can be visually
737 assessed from Figure 11. Furthermore, the parameters of specimens that were
738 discarded from the full dataset are in most cases obvious outliers. The ability to
739 identify these outliers can be used to recognise the faulty specimens during the
740 testing process, which requires a certain number of tested specimens to create a
741 representative statistical sample. Automating this procedure could contribute
742 to the reduction of unnecessary repeated testing by indicating the need for
743 additional tests in real time.

744 The parametrisation of load-displacement curves also allows us to analyse
745 the rate-dependence in each of the 12 parameters. The mean values of all
746 parameters in the reduced dataset, together with their standard deviation error
747 bars, are shown in Figure B.18. It can be seen that the parameters defining
748 the behaviour of the first branch, as well as the transitions between branches,
749 show some rate-dependent trends, whereas in the second and third branch these
750 trends are less obvious.

Loading speed (mm/min)	Specimen	Bondline thickness (mm)	Bond grade	$G_{II,c}$ (N/mm)	Discarded (if yes why?)
0.1	1	0.200	1	2.164	No
	2	0.203	3	2.640	No
	3	0.227	2	2.535	No
	4	0.173	1	1.696	Yes, grade
	5	0.333	3	4.731	Yes, thickness
	6	0.260	4	5.164	Yes, thickness
1	1	0.163	2	3.302	No
	2	0.087	2	2.346	No
	3	0.147	1	2.095	Yes, grade
	4	0.250	4	3.767	No
10	1	0.237	3	3.830	No
	2	0.213	1	3.753	No
	3	0.127	4	4.605	No
	4	0.277	3	7.022	Yes, thickness
100	1	0.193	4	4.743	No
	2	0.170	2	3.277	Yes, grade
	3	0.103	2	4.147	No
	4	0.207	2	3.825	No
1000	1	0.140	3	4.375	No
	2	0.167	2	4.072	Yes, grade
	3	0.127	4	5.630	No
	4	0.210	4	4.785	No
5000	1	0.113	3	4.145	No
	2	0.210	1	1.071	Yes, grade
	3	0.210	3	4.366	No
	4	0.123	1	3.527	No
	5	0.137	1	2.674	Yes, grade
	6	0.320	4	6.452	Yes, thickness
	7	0.297	4	6.438	Yes, thickness

Table A.3: Measured values of bondline thickness, bonding grade and $G_{II,c}$ for all specimens. Last column indicates whether the specimen was discarded from the reduced dataset, and if it was for what reason.

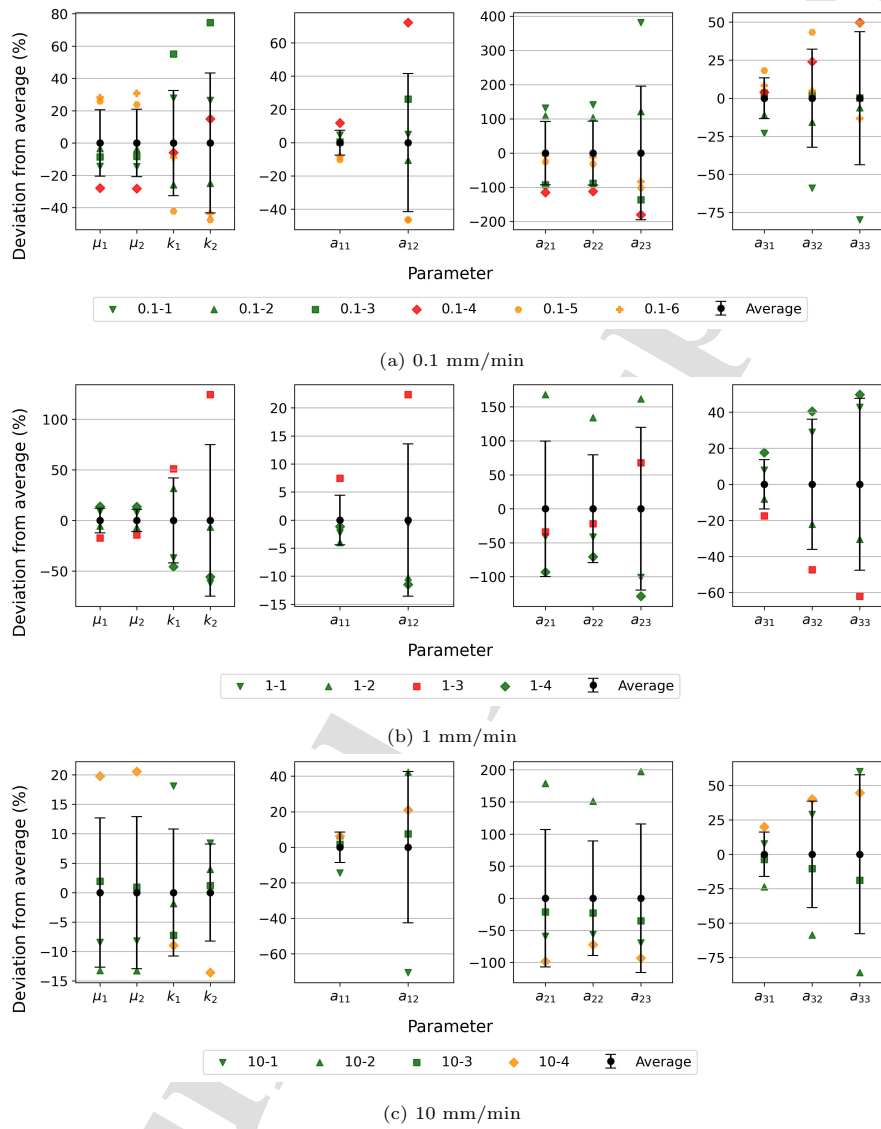


Figure B.16: Deviation from the average for the parameters used for the load-displacement curve parametrisation, separated by their respective branches for loading speed 0.1, 1 and 10 mm/min. Error bars are defined as relative standard deviations (RSD). Note the difference in deviation scales on the vertical axes.

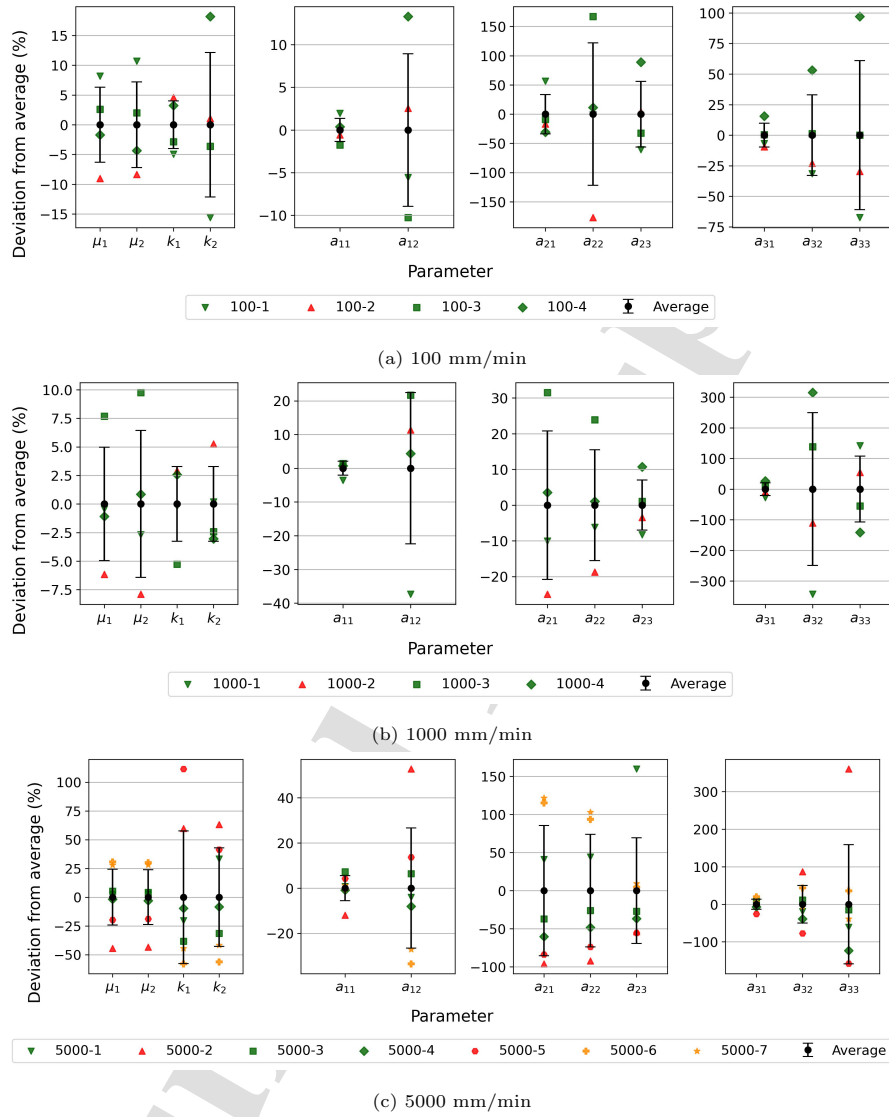


Figure B.17: Deviation from the average for the parameters used in the load-displacement curve parametrisation, separated by their respective branches for loading speed 100, 1000 and 5000 mm/min. Error bars are defined as \pm one relative standard deviation (RSD). Note the difference in the scale of the vertical axis.

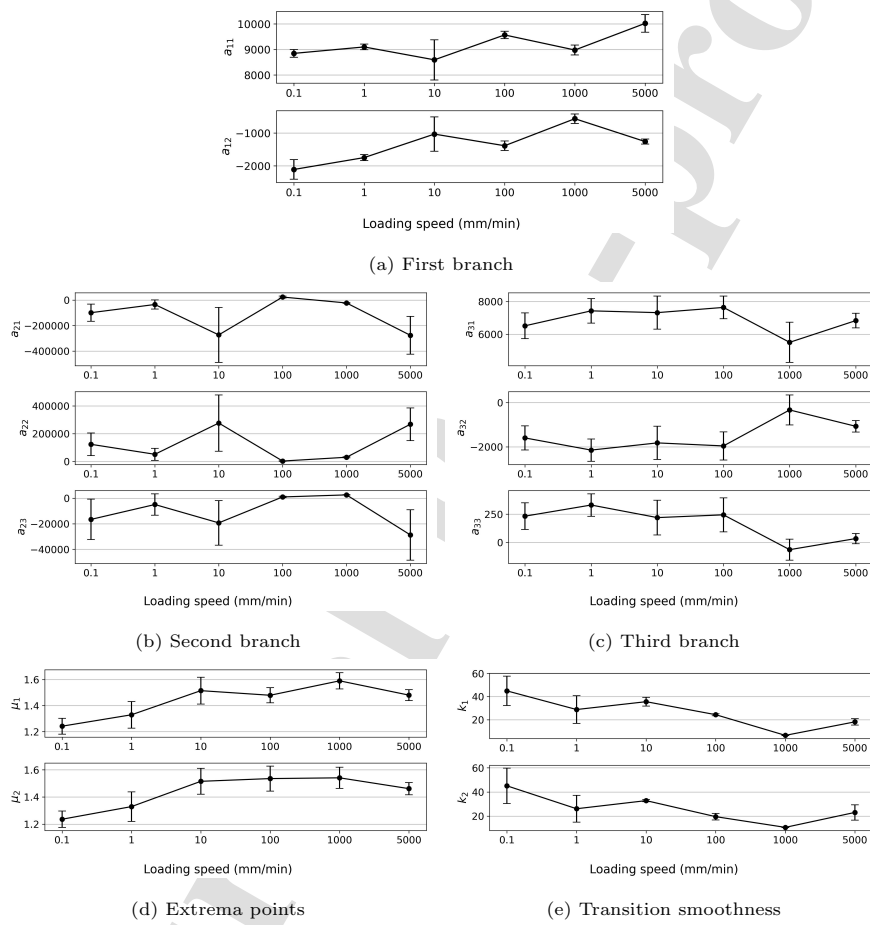


Figure B.18: Rate-dependant effects of each of the 12 parameters for reduced dataset. Note the difference in the scale of the vertical axis.

751 **References**

- 752 [1] A. Russell, K. Street, Moisture and Temperature Effects on the Mixed-
753 Mode Delamination Fracture of Unidirectional Graphite/Epoxy, ASTM
754 International100 Barr Harbor Drive, PO Box C700, West Conshohocken,
755 PA 19428-2959, 1985, pp. 349–370. doi:10.1520/STP36314S.
- 756 [2] J. Wang, P. Qiao, Novel beam analysis of end notched flexure specimen for
757 mode-II fracture, *Engineering Fracture Mechanics* 71 (2) (2004) 219–231.
758 doi:10.1016/S0013-7944(03)00096-1.
- 759 [3] M. De Moura, R. Campilho, J. Gonçalves, Pure mode II fracture charac-
760 terization of composite bonded joints, *International Journal of Solids and*
761 *Structures* 46 (6) (2009) 1589–1595. doi:10.1016/j.ijsolstr.2008.12.
762 001.
- 763 [4] L. F. M. Da Silva, F. A. C. R. G. De Magalhães, F. J. P. Chaves, M. F. S. F.
764 De Moura, Mode II Fracture Toughness of a Brittle and a Ductile Adhesive
765 as a Function of the Adhesive Thickness, *The Journal of Adhesion* 86 (9)
766 (2010) 891–905. doi:10.1080/00218464.2010.506155.
- 767 [5] Test Method for Determination of the Mode II Interlaminar Fracture
768 Toughness of Unidirectional Fiber-Reinforced Polymer Matrix Composites,
769 ASTM D7905/D7905M-14, ASTM International, West Conshohocken, PA,
770 USA, 2014.
- 771 [6] Aerospace Series. Carbon Fibre Reinforced Plastics. Test Method. Deter-
772 mination of Interlaminar Fracture Toughness Energy. Mode II. GIIC, BS
773 EN 6034:2015, BSI British Standards, London, United Kingdom, 2015.
- 774 [7] M. De Moura, A. De Morais, Equivalent crack based analyses of ENF
775 and ELS tests, *Engineering Fracture Mechanics* 75 (9) (2008) 2584–2596.
776 doi:10.1016/j.engfracmech.2007.03.005.

- 777 [8] T. O'Brien, Composite Interlaminar Shear Fracture Toughness, *G IIc:*
778 *Shear Measurement or Sheer Myth?*, ASTM International, 1998, pp. 3–
779 18. doi:10.1520/STP13263S.
- 780 [9] A. Arrese, N. Insausti, F. Mujika, M. Perez-Galmés, J. Renart, A novel
781 experimental procedure to determine the cohesive law in ENF tests,
782 *Composites Science and Technology* 170 (2019) 42–50. doi:10.1016/j.
783 *compscitech*.2018.11.031.
- 784 [10] B. Blackman, A. Kinloch, M. Paraschi, The determination of the mode
785 II adhesive fracture resistance, GIIC, of structural adhesive joints: An
786 effective crack length approach, *Engineering Fracture Mechanics* 72 (6)
787 (2005) 877–897. doi:10.1016/j.*engfracmech*.2004.08.007.
- 788 [11] B. Blackman, A. Kinloch, F. Rodriguez Sanchez, W. Teo, J. Williams,
789 The fracture behaviour of structural adhesives under high rates of testing,
790 *Engineering Fracture Mechanics* 76 (18) (2009) 2868–2889. doi:10.1016/
791 *j.engfracmech*.2009.07.013.
- 792 [12] F. Sun, R. Zhang, B. Blackman, Determination of the mode I crack tip
793 opening rate and the rate dependent cohesive properties for structural ad-
794 hesive joints using digital image correlation, *International Journal of Solids*
795 *and Structures* 217-218 (2021) 60–73. doi:[https://doi.org/10.1016/j.](https://doi.org/10.1016/j.ijsolstr.2021.01.034)
796 *ijsolstr*.2021.01.034.
- 797 [13] L. Škec, G. Alfano, Experimental and numerical study of rate-dependent
798 mode-I failure of a structural adhesive, *The Journal of Adhesion* 99 (8)
799 (2023) 1323–1355. doi:10.1080/00218464.2022.2106132.
- 800 [14] T. Carlberger, A. Biel, U. Stigh, Influence of temperature and strain rate
801 on cohesive properties of a structural epoxy adhesive, *International Journal*
802 *of Fracture* 155 (2) (2009) 155–166. doi:10.1007/s10704-009-9337-4.
- 803 [15] T. Carlberger, U. Stigh, Influence of Layer Thickness on Cohesive Proper-

- 804 ties of an Epoxy-Based Adhesive—An Experimental Study, *The Journal of*
805 *Adhesion* 86 (8) (2010) 816–835. doi:10.1080/00218464.2010.498718.
- 806 [16] B. Blackman, A. Kinloch, F. Rodriguez-Sanchez, W. Teo, The fracture
807 behaviour of adhesively-bonded composite joints: Effects of rate of test
808 and mode of loading, *International Journal of Solids and Structures* 49 (13)
809 (2012) 1434–1452. doi:10.1016/j.ijsolstr.2012.02.022.
- 810 [17] C. Borges, P. Nunes, A. Akhavan, E. Marques, R. Carbas, L. Alfonso,
811 L. Silva, Influence of mode mixity and loading rate on the fracture be-
812 haviour of crash resistant adhesives, *Theoretical and Applied Fracture Me-*
813 *chanics* 107 (2020) 102508. doi:10.1016/j.tafmec.2020.102508.
- 814 [18] M. Lißner, E. Alabort, B. Erice, H. Cui, B. R. K. Blackman, N. Petrinic, On
815 the dynamic response of adhesively bonded structures, *International Jour-*
816 *nal of Impact Engineering* 138 (2020) 103479. doi:10.1016/j.ijimpeng.
817 2019.103479.
- 818 [19] J. M. Guerrero, E. V. González, J. A. Artero, A. Cimadevilla, J. Rodríguez-
819 Sereno, J. A. Mayugo, E. De Blanpre, V. Jacques, Experimental and vir-
820 tual testing of mode II and mixed mode crack propagation under dynamic
821 loading, *International Journal of Impact Engineering* 193 (2024) 105042.
822 doi:10.1016/j.ijimpeng.2024.105042.
- 823 [20] W. Feng, Z. Li, B. Liu, C. Zhang, Evaluation of mode II fracture toughness
824 under high loading rate conditions for composite bonded joints, *Journal*
825 *of Adhesion Science and Technology* 37 (13) (2023) 1983–1996. doi:10.
826 1080/01694243.2022.2110656.
- 827 [21] S. Marzi, Measuring the critical energy release rate in mode II of tough,
828 structural adhesive joints using the tapered end-notched flexure (TENF)
829 test, *The European Physical Journal Special Topics* 206 (1) (2012) 35–40.
830 doi:10.1140/epjst/e2012-01584-4.

- 831 [22] M. May, O. Hesebeck, S. Marzi, W. Böhme, J. Lienhard, S. Kilchert,
832 M. Brede, S. Hiermaier, Rate dependent behavior of crash-optimized ad-
833 hesives – Experimental characterization, model development, and simula-
834 tion, *Engineering Fracture Mechanics* 133 (2015) 112–137. doi:10.1016/
835 j.engfracmech.2014.11.006.
- 836 [23] M. Lißner, E. Alabort, H. Cui, R. Rito, B. Blackman, N. Petrinic, Ex-
837 perimental characterisation and numerical modelling of the influence of
838 bondline thickness, loading rate, and deformation mode on the response of
839 ductile adhesive interfaces, *Journal of the Mechanics and Physics of Solids*
840 130 (2019) 349–369. doi:10.1016/j.jmps.2019.06.011.
- 841 [24] M. Pérez-Galmés, J. Renart, C. Sarrado, A. Brunner, A. Rodríguez-Bellido,
842 Towards a consensus on mode II adhesive fracture testing: Experimen-
843 tal study, *Theoretical and Applied Fracture Mechanics* 98 (2018) 210–219.
844 doi:10.1016/j.tafmec.2018.09.014.
- 845 [25] J. C. P. Figueiredo, R. D. S. G. Campilho, E. A. S. Marques, J. J. M.
846 Machado, L. F. M. da Silva, Adhesive thickness influence on the shear
847 fracture toughness measurements of adhesive joints, *International Journal*
848 *of Adhesion and Adhesives* 83 (2018) 15–23. doi:10.1016/j.ijadhadh.
849 2018.02.015.
- 850 [26] K. Alfredsson, On the instantaneous energy release rate of the end-notch
851 flexure adhesive joint specimen, *International Journal of Solids and Struc-*
852 *tures* 41 (16-17) (2004) 4787–4807. doi:10.1016/j.ijsolstr.2004.03.
853 008.
- 854 [27] Abraham. Savitzky, M. J. E. Golay, Smoothing and Differentiation of
855 Data by Simplified Least Squares Procedures., *Analytical Chemistry* 36 (8)
856 (1964) 1627–1639. doi:10.1021/ac60214a047.
- 857 [28] Y. Mi, M. A. Crisfield, G. A. O. Davies, H. B. Hellweg, Progressive Delam-
858 ination Using Interface Elements, *Journal of Composite Materials* 32 (14)
859 (1998) 1246–1272. doi:10.1177/002199839803201401.

- 860 [29] R. H. Byrd, P. Lu, J. Nocedal, C. Zhu, A Limited Memory Algorithm for
861 Bound Constrained Optimization, *SIAM Journal on Scientific Computing*
862 16 (5) (1995) 1190–1208. doi:10.1137/0916069.
- 863 [30] M. De Moura, M. Silva, A. De Morais, J. Morais, Equivalent crack based
864 mode II fracture characterization of wood, *Engineering Fracture Mechanics*
865 73 (8) (2006) 978–993. doi:10.1016/j.engfracmech.2006.01.004.
- 866 [31] R. Serpieri, E. Sacco, G. Alfano, A thermodynamically consistent deriva-
867 tion of a frictional-damage cohesive-zone model with different mode I and
868 mode II fracture energies, *European Journal of Mechanics - A/Solids* 49
869 (2015) 13–25. doi:10.1016/j.euromechsol.2014.06.006.

Highlights

- A novel method for the parametrisation of the load-displacement curves in ENF tests is presented
- An average curve can be constructed by averaging parameters of individual curves
- Rate-dependent effects beyond those of $G_{II,c}$ can be quantitatively assessed
- The analysis of parameters enables scatter assessment and detection of faulty specimens
- Average curves can improve the identification of the input parameters of non-linear numerical models

Declaration of interests

The authors declare that they have no known competing financial interests or personal relationships that could have appeared to influence the work reported in this paper.

The authors declare the following financial interests/personal relationships which may be considered as potential competing interests:

Journal Pre-proof